The Pennsylvania State University
The Graduate School

OBSERVATIONAL CONSEQUENCES OF GRAVITATIONAL WAVE EMISSION FROM SPINNING COMPACT SOURCES

A Thesis in
Physics
by
David M Whitbeck

© 2006 David M Whitbeck

Submitted in Partial Fulfillment
of the Requirements
for the Degree of

Doctor of Philosophy

August 2006

The thesis of David M Whitbeck was reviewed and approved* by the following:

Benjamin J. Owen
Assistant Professor of Physics
Thesis Advisor, Chair of Committee

Lee Samuel Finn
Professor of Physics, Professor of Astronomy and Astrophysics

Pablo Laguna
Professor of Astronomy and Astrophysics, Professor of Physics

Michael Eracleous
Associate Professor of Astronomy and Astrophysics

Jayanth R. Banavar
Professor of Physics
Head of the Department of Physics

*Signatures are on file in the Graduate School.

Abstract

This thesis covers two distinct projects on gravitational wave physics. The first project is a mathematical computation of the gravitational radiation recoil from spinning black hole binary mergers. Radiation recoil speeds have important implications in several astrophysical scenarios such as black hole ejection from globular clusters and dwarf galaxies, hierarchical formation of black holes and more. The inability to directly measure this effect means that theoretical predictions offer the only insight into the size and importance of radiation recoil in the aforementioned astrophysical scenarios. The result found is that spin has the effect of reducing the recoil. Furthermore, the recoil speed is bounded above by roughly 100 km/s.

The second project details computing the Fisher information matrix and parameter space search metric for spinning down periodic sources using a simple "Ptolemaic" model of the Earth's orbit. This is then used to determine the optimal grid for the LIGO periodic sources group to search for unknown pulsar signals. The grid is implemented under the distributed computing project Einstein@Home to search LIGO data for periodic signals from previously unknown objects over the entire sky and frequency band. It has been used by Einstein@Home since summer 2005, for the S4 and now the S5 data runs.

Table of Contents

List of Figures

List of Tables

Acknowledgments

I am most grateful to my adviser Ben Owen for finding and giving me these interesting and important projects. Both of these projects were completed mutually between us, and the frequent meetings were very helpful.

I am also grateful to Ian Jones, who worked with Ben and me on the LIGO pulsar information matrix project. If it wasn't for him I think that progress might have proceeded at a slower pace on that project.

I would like to thank the following faculty that served on either my pre-comprehensive committee, comprehensive committee, or my thesis committee: Bernd Bruegmann, Doug Cowen, Steinn Sigurdsson, Sam Finn, Mike Eracleous, and Pablo Laguna. They have provided me with many helpful comments. In particular I wish to thank Ben Owen, Sam Finn for their considerable comments, proofreading and advice. I also wish to thank Mike McCaffrey for taking the time to carefully proofread my thesis as well. Any errors that are made in this thesis are purely my own and no others.

I would also like to thank my friends Doug Rutledge, Tim Bramfeld, Mohit Nayyar, Mike McCaffrey, Steve Molino, John "Anthony" Taylor, Mike Demster Brook, and Karl Henning. You guys really helped keep me sane over the past five years. Finally, I would like to thank my family for being so supportive.

The research presented in this thesis was supported by National Science Foundation grants PHY-0245649 and PHY-0555628 and by PHY-0114375 (the Penn State Center for Gravitational Wave Physics).

Chapter 1

Introduction

1.1 Overview

This thesis addresses two very different problems concerning observational consequences of gravitational wave emission from spinning compact sources. The first estimates the astrophysical significance of gravitational radiation recoil and the second addresses a practical problem in searching for the waves themselves.

Gravitational waves emit linear momentum, just as they emit energy and angular momentum. This can lead to black holes produced from binary black hole mergers acquiring a "recoil" velocity from conservation of linear momentum. This is important because there are many significant astrophysical consequences if the recoil velocity is high enough. In Chapter 2 of this thesis, the momentum flux is analytically computed using a perturbative method known as the post-Newtonian expansion. Then the net recoil is found by numerically integrating the linear momentum flux using analytic models to approximate each phase of the orbital history. It is one of the first attempts to consider the effects of spin in computing the recoil speed. The result is that the presence of nonzero spin decreases the recoil, yielding recoil speeds bounded by 100 km/s. While the recoil is a theory project that can be used to make inferences about astrophysical phenomena, the second project, outlined in chapter three, is a data analysis project that will aid in making detections.

Searching for gravitational wave events in LIGO (Laser Interferometer Gravitational Wave Observatory) can be done by "matching" the signal against theoretical

template waveforms. In particular, the search for gravitational waves from previously undetected neutron stars can be done this way but can be prohibitively computationally expensive. For that reason a finite set of templates must be chosen to maximize the odds of finding a signal for a fixed computing budget. In Chapter 3 the solution to that problem is found using a statistical method known as maximum likelihood. The templates are parameterized. The problem then becomes finding the best grid over the parameter space to use. There is an object called the Fisher information matrix that quantifies how much the likelihood is affected by choosing a finite grid spacing. The information matrix is analytically computed using a set of simplifying assumptions. From the information matrix the templates chosen for the unknown pulsar search are determined numerically. In Chapter 3 the Fisher information matrix for the "unknown pulsar search" is analytically computed. Another matrix, derivable from the information matrix, called the pulsar search metric is then computed. The results of this computation were coded in the LSC (LIGO Science Collaboration) Algorithms Library (LAL) software environment and tested using LAL and LALApps (a suite of applications using LAL). The grid on the parameter space has been used by Einstein@Home for the LIGO all-sky periodic sources search for about a year now.

1.2 Radiation Recoil from spinning black hole mergers

We begin by discussing why radiation recoil from spinning black hole mergers is an important problem. Accurately computing gravitational radiation recoil has been desirable because there are a host of interesting astrophysical phenomena that would result from significant recoil velocities produced from binary mergers. Over the past few decades there have been many attempts to compute it both analytically and numerically. The resulting upper bounds have varied by orders of magnitude. These bounds are still hotly debated to this day. Nearly all of the work has focused on non-spinning binaries, but a paper two years back by Favata *et al.* [1] suggests that spin has an important effect on the size of the recoil velocity. This motivated the project done in Chapter 2.

1.2.1 Astrophysical consequences

During binary black hole mergers linear momentum is lost through gravitational wave emission. Thus the final black hole produced from a merger acquires a recoil velocity. This effect can have important consequences for various astrophysical scenarios depending on how fast these recoils are. Some of these scenarios were explored in detail by Merritt *et al.* [2]. In globular clusters if black holes can acquire recoil speeds that are higher than the escape velocity of the globular cluster, they might then leave the cluster. We would then expect that these ejections may play a significant role on the dynamics of globular clusters. More importantly, if globular clusters can not retain black holes, then the expected event rates for intermediate mass black hole binary mergers will be significantly reduced. This is important because intermediate mass black hole mergers are candidates for detection by both advanced LIGO and LISA [3, 4] . The recoil speed needs to attain values up to $10 - 100$ km/s for black holes to become unbound from globular clusters. The same effect of black hole ejections can also occur for dwarf galaxies. In this case the recoil speeds need to attain values of $10 - 100$ km/s for dwarf galaxies, and $300 - 1000$ km/s for elliptic galaxies for ejections to occur [2]. Dark matter halos might also have trouble retaining black holes. This has important implications for hierarchical models used to explain the creation of supermassive black holes. If the recoil speed can attain values up to $150 - 300$ km/s, then the maximum redshift z for confining black hole progenitors in a dark matter halo will be $z \lesssim 10$. The implication of this result is that seeding from black holes that start earlier than $z \sim 10$ are disfavored. One then reaches the conclusion that hierarchical formation of supermassive black holes is disfavored by radiation recoil [5]. Radiation recoil could also displace nuclei from the centers of galaxies with long infall times, arbitrarily long for dwarf galaxies, explaining the observed mass deficits in the centers of some bright galaxies [2].

There are also some new interesting observational consequences of recoil that were explored in the wake of Merritt *et al.* [6]. In particular the quasar HE450-2958, discovered by Magain *et al.* has been claimed by them to be without a detectable host galaxy, may be a supermassive black hole which became unbound due to recoil [6]. If that is true, it would be the first identification of a binary black hole merger involving a supermassive black hole. It also would suggest that rapid

merging of supermassive binaries is widespread and that the rate of detection of such events by the Laser Interferometer Space Antenna (LISA) is favorable [7]. However, the claim has been contested by Merritt *et al.* [8]. Furthermore Merritt *et al.* claim that gravitational radiation recoil speeds must exceed 500 km/s to be a viable mechanism of ejecting the quasar from its host galaxy. If gravitational radiation recoil is large enough, it will also disfavor hierarchical formation of supermassive black holes [5] due to dynamical friction not being strong enough to retain kicked black holes. Then the discovery of luminous quasars at redshift $z \geq 6$ by the Sloan Digital Sky Survey would suggest that the black hole seeds grew at super-Eddington rates [9]. This has been further quantified by Volonteri and Rees: super-Eddington growth must occur for $z = 6$ quasars that have host halo masses of at least $10^{13} M_{\odot}$ [10]. To properly understand how recoil influences these astrophysical phenomena, we need accurate figures for how large these recoil velocities can typically be. Unfortunately the different attempts to compute radiation recoil over the years have varied by orders of magnitude.

1.2.2 History of radiation recoil

Linear momentum flux from gravitational waves (and electromagnetic waves) was first computed by Peres to leading order [11] in 1962, and independently by Bekenstein in 1972 [12]. The net radiation recoil from leading order linear momentum flux for Keplerian orbits was first computed by Fitchett [13] in 1982. This is the first numerical estimate of the recoil velocity, and the recoil speed was found to be bounded by 1480 km/s with an extremely large margin of uncertainty. Fitchett and Detweiler computed the recoil for extreme mass ratio binaries using a technique known as black hole perturbation theory. They found the upper bound to be 125 km/s [14]. The post-Newtonian correction for the linear momentum flux was computed by Alan Wiseman [15] in 1992. The correction greatly decreased the recoil. In recent years there have been many publications on computing radiation recoil. Kidder found the leading order post-Newtonian spin contribution to the linear momentum flux [16]. Favata *et al.* also investigated spin effects, but using black hole perturbation theory. They found that by including spin effects the recoil speeds have an upper bound of roughly 500 km/s [1]. Blanchet *et al.* computed

the 2PN (second order post-Newtonian) expression for the linear momentum flux without spin, and found the recoil is bounded by roughly 250 km/s [17]. Damour and Gopakumar used the effective one body formalism to compute the recoil for nonspinning binaries, and obtained an upper bound of 74 km/s [18]. Baker *et al.* using numerical relativity obtained a result that lies roughly midway between Blanchet *et al.* and Damour and Gopakumar [19]. Another numerical relativity result by Herrmann *et al.* suggests that the recoil speeds can be well in excess of 100 km/s [20]. So we see that the resulting figures for the recoil least upper bound have varied by roughly an order of magnitude, although they are trending lower in recent years. Those results where upper bounds were placed are summarized in Table 1.1. There currently is no consensus on the size of the recoil speed. And just as importantly, there has been little work on addressing the effect of spin, but what work there is points to it having a significant impact on recoil. Since we expect that most black holes will be spinning, it behooves us to investigate further.

1.2.3 The importance of spin effects

Out of those results discussed, the publication by Favata *et al.* [1] suggests that spin can strongly affect the size of the recoil speed. Their figures have the recoil speed attaining values that make it astrophysically interesting for the scenarios considered in the previous section. In Chapter 2 an alternative method is used, which relies upon assumptions that complement the ones assumed by Favata *et al.*'s application of black hole perturbation theory. We are the first to compute the linear momentum flux to 2 PN order for *spinning* black holes with arbitrary mass ratio. The integration of the linear momentum flux is partially done in the spirit of Blanchet *et al*'s [17] and Damour and Gopakumar's [18] method for non-spinning binaries. However, their methods for modeling the plunge for spinning black holes did not carry over well. More sophisticated modeling of the transition and plunge phases of the orbit were needed. The transition phase between the adiabatic inspiral phase and the plunge phase is computed here in the manner of Ori and Thorne [21], with a few innovations. The recoil project was far more involved than the data analysis project, but the latter project is just as important for very different reasons.

Authors	Date	Upper Bound (km/s)
Fitchett	1982	1480
Fitchett *et al.*	1984	120
Favata *et al.*	2004	500
Blanchet *et al.*	2006	250
Damour and Gopakumar	2006	74

Table 1.1. History of the predicted upper bounds on the recoil

1.3 LIGO periodic sources search

To search for and identify unknown pulsar sources in the Laser Interferometer Gravitational-Wave Observatory (LIGO), an optimal grid on the parameter space is needed. In Chapter 3 the pulsar search metric was computed, and a grid over the parameter space was found from it.

Pulsars are believed to emit detectable gravitational radiation based upon several proposed mechanisms such as r-modes or mountains supported by elastic or magnetic stresses [22, 23, 24]. Pulsar signals are modeled by Doppler shifted slowly evolving sinusoids. There are several methods that have been developed to search for pulsar signals in LIGO data, all of which should eventually use the grid developed in Chapter 3. All of these methods are too computationally intensive to run on a cluster if a data set of worthwhile length is used. For that purpose a distributed computing program called Einstein@Home has been developed and used by tens of thousands of users to search LIGO data for periodic signals.

1.3.1 Brief overview of LIGO

LIGO (the Laser Interferometer Gravitational-wave Observatory) consists of three Earth based interferometers built to detect gravitational waves. Let us consider a simple model of the Michelson interferometer (as shown in Figure 1.1) to illustrate how interferometers detect gravitational waves. When a gravitational wave passes through the interferometer, the lengths of the arms will change sinusoidally with time and 180 degrees out of phase with each other. Accordingly, it takes longer for wavefronts to travel down one arm than it would the other. This introduces a phase offset between the two beams when they recombine. The interference pattern of

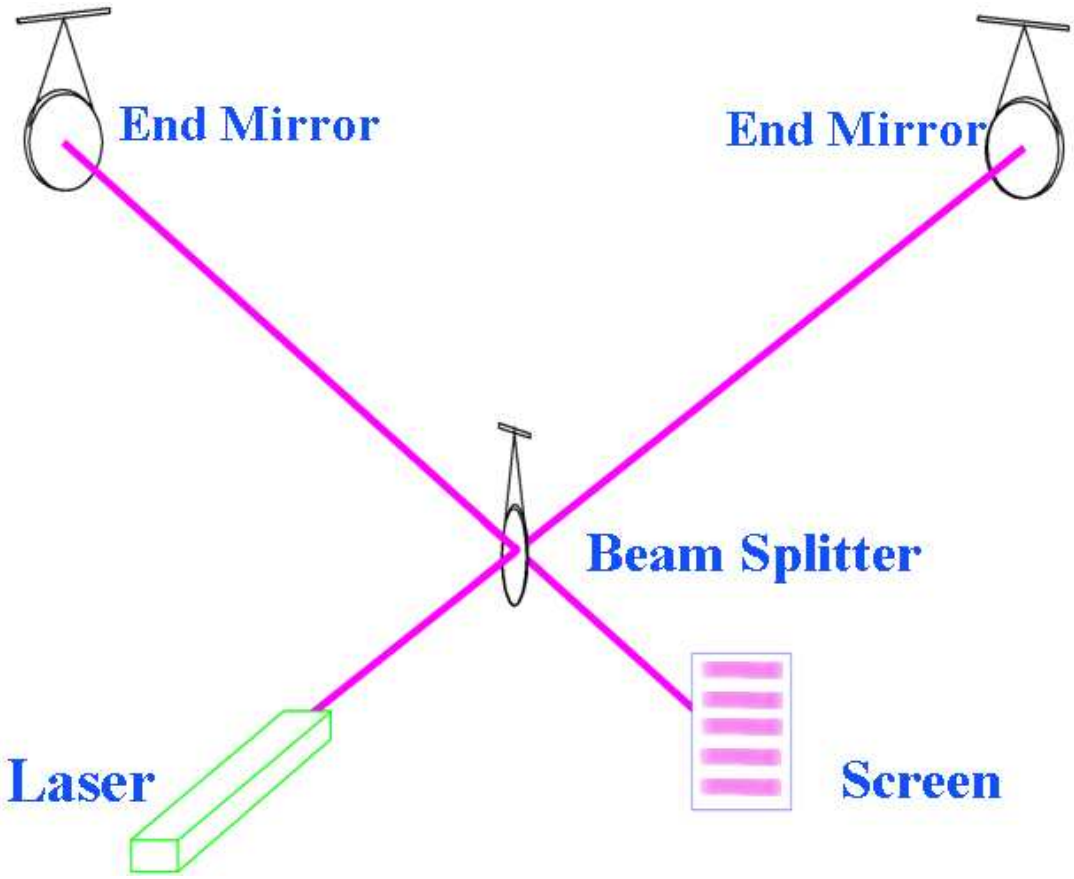

Figure 1.1. Illustration of Michelson interferometer. Credit LSC

the two beams is then expected to change if a gravitational wave passes through the detector. LIGO is not really a Michelson interferometer, but the concept behind how it works is the same. The real interferometers recycle the power with Fabry-Perot cavities to achieve greater sensitivity to the expected faint gravitational wave signals. They are also quite sensitive to noise.

Finding and identifying signals in noisy data is a challenge that must be met to detect gravitational waves. The challenge has been met in other scientific and engineering fields and while some methods carry over to gravitational waves some new methods must be developed to meet the needs of this emerging field. The LSC (LIGO Science Collaboration) was organized in the 1990s (while LIGO was under construction) to do this, among other things, and has worked for many years on developing the data analysis tools. Within the LSC are four sub-groups working on data analysis development and implementing searches for four types of signals. The

methods employed to search for and identify gravitational wave events in LIGO data depend on the nature of the source of the signal. And there are several types of signals that we might expect to find. For practical (data analysis) purposes they are divided into unmodeled bursts, compact binary inspirals, the stochastic background and periodic sources.

Bursts are gravitational wave events of short duration. They are expected from core collapse of stars, binary black hole mergers and gamma ray bursts [25] among others. These signals are unmodeled and are found by triple coincidence searches. A stochastic background is produced from a superposition of uncorrelated cosmological and astrophysical sources such as primordial gravitational waves from the early universe and many faint supernova bursts from the entire subsequent history of the universe. It is measured by cross-correlating data streams from two different interferometers [26]. The compact binary inspiral search tries to detect black hole and neutron star binary mergers. This is done by matched filtering, where the signals are compared to post-Newtonian or other model waveforms in much the same way that the F-statistic search works for periodic sources [27]. Data analysis work on all these searches is urgently needed because (i) methods for some types of search are not completely developed and (ii) implementation of even the simplest searches has not yet caught up with data taking.

Analyzing data from LIGO is challenging because the faint signals from gravitational waves are buried in noise. The LSC (LIGO Science Collaboration) has been working on developing the tools for this task for nearly a decade now. Despite the tremendous amount of work that has been done, there is still much to do. The LIGO sensitivity has jumped by leaps and bounds, as illustrated in Figure 1.2. LIGO has finally reached the initial design sensitivity goal, as demonstrated in the S5 (fifth science run) sensitivity curve in Figure 1.3. The goal of this run is to accumulate a year of triple coincidence data which is projected to happen in early 2007. Nearly eight calendar months of data have been taken as of this writing, but due to the duty cycles of the instruments the triple coincidence time is less. S5 is by far the longest science run so far, and it is also the most sensitive. The problem is that not all of the analysis software is developed sufficiently to fully exploit this potential goldmine of data. There remain numerous LIGO data analysis problems that have now become urgent. Chapter 3 addresses one of them, whose urgency

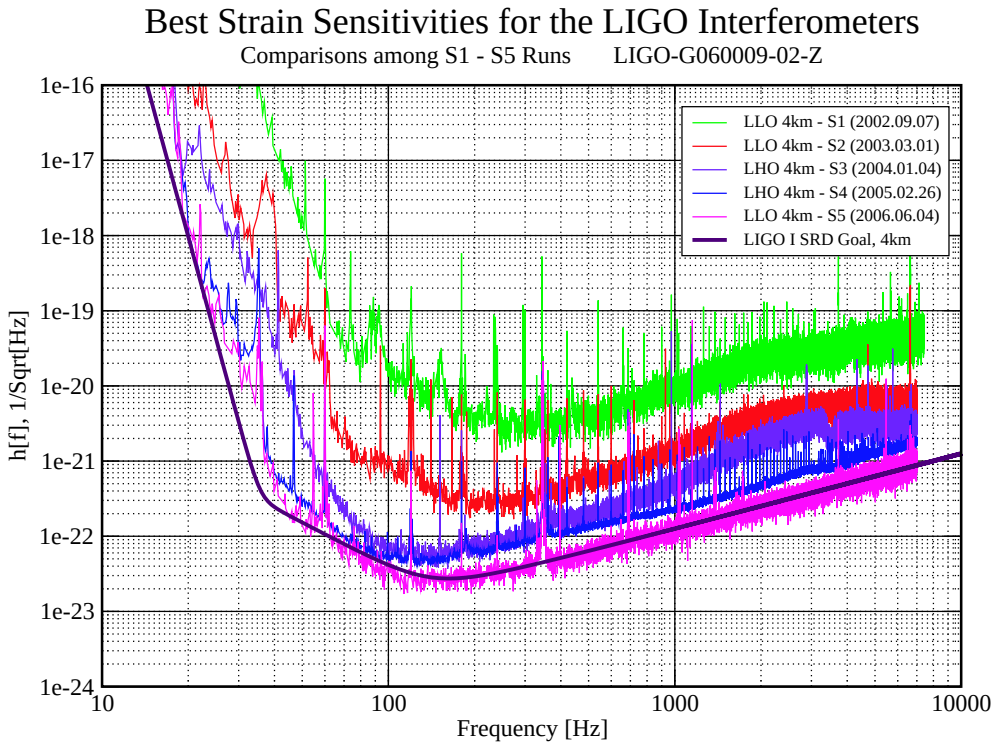

Figure 1.2. Strain sensitivities of the LIGO interferometers S1-S5 (early), credit LIGO Lab Document G060009-02

can is shown by the fact that it involves the vast majority of the computing power available to the LSC. Determining the grid for an unknown pulsar search was an important stepping stone for the search methods in development. The search itself is important because in recent years there have been many plausible mechanisms for pulsars to emit detectable gravitational waves; even at the level where initial LIGO might actually detect a pulsar signal [28].

1.3.2 Gravitational wave emission mechanisms

There have been several proposed mechanisms to produce periodic, persistent, gravitational waves from rotating neutron stars. Deformations or mountains on the crust of the neutron star are one such mechanism. These deformations could be created in either of two ways. They can be created by shear stresses in the

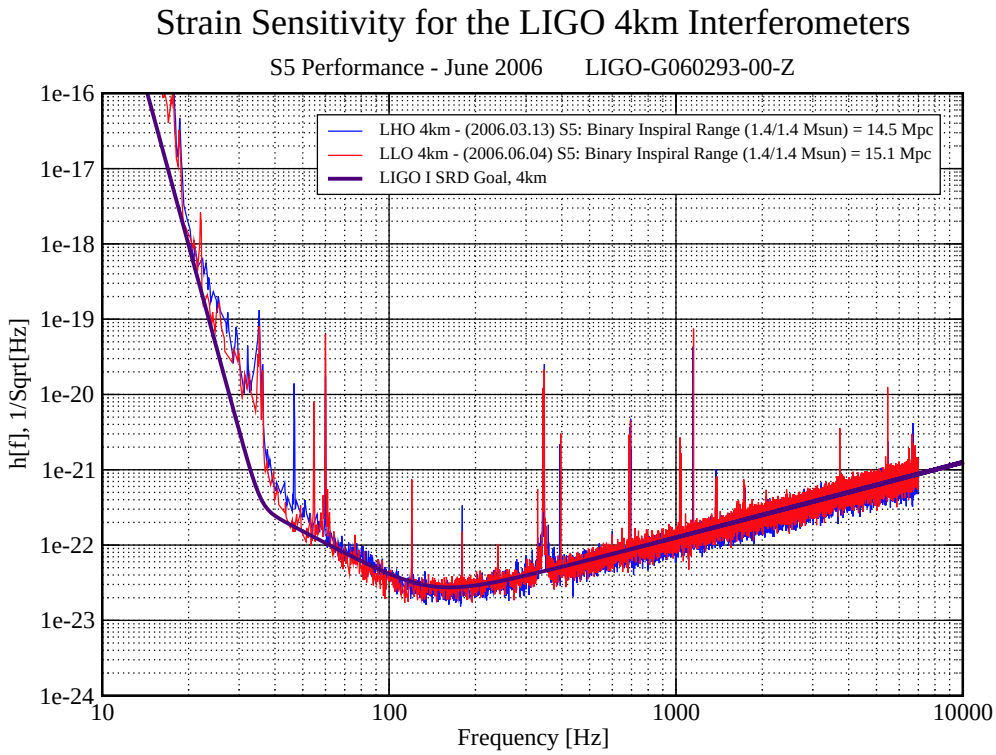

Figure 1.3. Strain sensitivity of the LIGO interferometers from the S5 run, credit LIGO Lab Document G060293-00

crust. Elastic deformations in strange quark or hybrid baryon-quark stars can produce ellipticities high enough to be detected by initial LIGO [24]. The deformations can also be created by accreted matter from a companion being pinched up by the large magnetic field of the neutron star. They can also be created by thermal elastic mountains. Toroidal magnetic fields in neutron stars can rotate to be orthogonal to the rotation axis, pinching matter making the neutron star triaxial [23]. Another way is by modes of fluid oscillation in the neutron star called r-modes. These modes are dominated by the Coriolis force, and are unstable to gravitational wave emission [29]. Freely precessing neutron stars can also generate gravitational waves [30].

These are all plausible scenarios that provide explanations of why we might expect to detect periodic sources with either initial LIGO or advanced LIGO. Therefore it is important to search for these signals. It has been argued [31] that,

regardless of emission mechanism, the expected maximum amplitude on the strain on the detector will be comparable ($h_0 \sim 4 \times 10^{-24}$) to the sensitivity of LIGO if ran for a year [31]. So to reiterate, it might be possible for initial LIGO to detect periodic signals from exotic alternatives to standard neutron stars [24]. At the very least the upper limits placed by S5 will start to become interesting because some signals could have been detected. Consequently, several methods have been swiftly developed to efficiently search LIGO data for periodic sources.

1.3.3 LIGO periodic sources search

There are three types of searches that the LIGO periodic sources group does There is a fourth searching for signals from rapidly accreting neutron stars such as Sco X-1 [31], but since it could only detect something with advanced LIGO we do not discuss it further here. The three are the the known pulsar search, the directed search for known non-pulsating neutron stars, and the unknown pulsar search. The known pulsar search does not search over the parameter space, because the parameters are already known from radio or x-ray pulsar observations. For the directed search, for non-pulsing neutron stars the positions of the sources are known. Therefore, only the spindown parameters and frequency are searched over. The unknown pulsar search explores the entire parameter space. There are three principal search methods used for the latter search. These are the stack-slide method, the Hough transform and the Powerflux method.

Searching for known pulsars is different from the other searches. This is because the intrinsic parameters are already known. The signal is multiplied by a waveform with exactly the opposite expected phase evolution [32]. This is known as heterodyning the data. What remains is the antenna beam pattern modulation of the amplitude. The remaining parameters that must be fit to identify a known source are the amplitude, inclination angle, polarization angle and phase offset.

Directed searches for known non-pulsating neutron stars are based upon searching over the frequency and spindown parameters only, since the sky positions of the candidates are already known. Searching over a much smaller parameter space, directed searches are not nearly as computationally intensive as the full unknown pulsar search. The two obvious candidates for such a search would be the neutron

star in the supernova remnant Cas A and RX-J1856, but there are several others. Cas A might be the youngest known non-pulsating neutron star, and has the highest limit on the strain amplitude. However the weaker candidate RX-J1856 is the nearest neutron star, and would not be as computationally intensive to search for.

There are three search methods for unknown pulsars, all of which are incoherent hierarchical searches. The first pass of a hierarchical search is done over short stretches of data on a coarse grid, using a low threshold for the signal-to-noise. Subsequent passes only search the candidates of the previous passes. These searches are done on a finer scale. They are also done over longer stretches of data, which increases the computational cost per unit parameter space. But because only the neighborhoods of candidates are searched, the total computational cost is manageable. There will be many false alarms on the first pass, but there is an advantage of being able to detect weaker signals that might have been otherwise ignored. The passes using a finer grid will weed out the false alarms triggered from the first pass.

The stack-slide search works by dividing the data into many short Fourier transformed sections. A short Fourier transform (SFT) is a Fourier transform done over a short enough time that the frequency does not change much. First a coarse grid search is done on each SFT. What follows is a description of how the fine grid search is done. A point is chosen on the fine grid. From it the barycentered time difference (i.e., with the Doppler shifts due to the Earth's rotation and orbit removed) for each SFT is computed. This is used to correct for the evolution of the spindown parameters across each SFT. And thus the phase shift over each SFT is corrected accordingly. The power spectra are shifted to correct for the frequency drift over each SFT. This is called sliding. If the template associated with the parameter matched well, then the signals will line up from each SFT. Now the power spectra can be simply added or "stacked". Clearly this is an incoherent summation, and so this type of search is called an incoherent search. The result is searched for spikes above a specified threshold indicating a potential signal [33].

Another important search is the Hough transform. The Hough transform search is based upon the stack-slide. The power is analyzed in a less obvious but more robust way. After sliding, the power spectrum is transformed into a binary sequence. The Hough transform works by assigning the number one to frequency

bins where the power is above a specified threshold, else the number zero is assigned. Transforming the data this way allows one to tabulate a set of points $\{x_i\}$ of these candidates with the coordinates being frequency and time. There are many templates that pass through an individual point. So each point $\{x_i\}$ has an associated curve $\{U_i\}$ in the parameter space. Theoretically if the signal exactly matched a template, the intersection of these curves would be the point in the parameter space whose template contained the set of observed $\{x_i\}$. But in real life, some of the observed events in the frequency bins were triggered due to noise. Therefore, some of the points do not belong to true signals. What then must be done is to compute the number of curves passing through each point on the grid. This is essentially the Hough transform. The Hough transform maps the data onto a histogram on the parameter space [34]. It is less efficient than the stack-slide, but it is more robust against non-Gaussian excursions of the noise.

The third and most efficient type of incoherent search is the Powerflux [35]. Like the Hough, it is also based upon the stack-slide search. The power spectra from the SFTs are weighted against the average power spectrum and the antenna beam pattern. One of the advantages of Powerflux is to allow direct parameter estimation without the aid of Monte Carlo simulations. This is because the transformation of the power as outlined above is a direct measure of the power output due to the source. The Powerflux method is a frequentist analysis that puts 95% confidence limits on the gravitational wave flux across the sky [36].

All of these search methods are designed to be computationally efficient. However, the analyses are done over so much data that it is still very impractical to run the analysis on a typical cluster. Many more CPU resources were needed. They were found in a distributed computing program similar to SETI@Home called Einstein@Home.

1.3.4 Einstein@Home

The computational cost of coherently analyzing long stretches of data searching for unknown periodic sources is expensive, and increases with observation time. For observation times of days, which are needed to perform the search effectively, it quickly becomes too taxing for a modest cluster to make interesting conclusions.

For this reason a project called Einstein@Home was created. Einstein@Home uses the same software (BOINC) as is used by the SETI@Home project. The idea is to offer a screensaver for people to use. The screensaver analyzes data when their computers are not being used. The combined power of tens of thousands of users means that the analysis can be run much faster. Einstein@Home is now effectively a 60 teraflop computer created by combining 70,000 desktop computers. And it uses a substantial fraction of a million dollars of electricity per month.

The LIGO data must be prepared in packets to send out to the users. The following outlines the procedure to do that. The data is broken up into half hour segments. For instance, in the third science run (S3) there were 600 hours of selected data. From that there are 1200 half hour segments. Each segment is Short Fourier transformed. The frequency band $50 - 1500$ Hz is divided up into sections of .8 Hz. These sections overlap so that the signal isn't lost due to frequency drift (intrinstic or from Doppler shifts). The coherent integrations were done over 10 hour stretches. The analysis of each of these data sets is done independently by multiple computers, and if the same results are found, the analysis is validated and the users receive credits for their work [37]. The screensaver shows the progress of the search with a rotating celestial sphere and a moving target indicating the sky position currently being analyzed. The grid on which that target moves, an integral part of the analysis which users frequently ask about on the Einstein@Home web forums, is computed using the results of Chapter 3 of this thesis. At present, data from different 10 hour sections are combined in a way that produces a histogram on the sky. This method is similar to the Hough method, but it is much simpler. One of the more sophisticated hierarchical searches will be implemented by Einstein@Home in the future.

Chapter 2

Radiation Recoil

Gravitational radiation recoil may be an important mechanism for black hole ejections from globular clusters and displacement of nuclei of dwarf galaxies. For spinning binary black hole mergers recoil can be significant even when the black holes have comparable mass. We compute the momentum flux due to gravitational wave emission from a spinning non-precessing black hole binary with a circular orbit to second post-Newtonian order. The maximum recoil velocity near the innermost stable circular orbit (ISCO) is reduced from the non-spinning case by tens of percent for retrograde orbits and enhanced by a factor of up to three for prograde orbits. We estimate the recoil due to the plunge from the ISCO to the formation of a common horizon based on the Ori-Thorne approximation to a plunge geodesic in the Kerr spacetime. Like the recoil at ISCO, the final recoil (which is dominated by the plunge) is enhanced for prograde orbits and reduced for retrograde orbits. Counterintuitively, the effect depends not so much on the effective Kerr parameter as on another spin parameter corresponding to the alignment of the spins unless the Kerr $|a/M|$ is near its maximum (where the results are hard to trust). Away from that maximum, we find recoil velocities up to 100 km/s, but this is highly dependent on the form of the momentum flux near the horizon.

A more technical survey of the recent work and its relation to the research done here will be outlined here in greater detail than in Chapter 1. Furthermore, qualitative descriptions of the mathematical methods employed in computing the recoil will be developed and explored. The conceptual differences between the spacetimes of spinning black holes will be compared and contrasted with that

of nonspinning black holes to illuminate the challenges inherent in treating spin. The post-Newtonian expression for the linear momentum flux is computed, and the result explored in a few special cases. The integration is then done, and the resulting recoil plotted in contour plots across the parameter space. The results are discussed in relation to the previous work done on recoil.

2.1 Introduction

The recent interest in gravitational radiation recoil was kindled by a calculation by Favata, Hughes, and Holz [1] (hereafter referred to as FHH). FHH used perturbation theory of spinning black holes to estimate that final recoil velocities could easily exceed 200 km/s and in some cases might approach 500 km/s. (Such a calculation was first done for non-spinning black holes by Fitchett and Detweiler [14], who estimated a maximum recoil velocity above 125 km/s.) The key assumption in this method is that one hole is much less massive than the other, although the largest and thus most interesting recoil velocities are for mass ratios about 1:2. The final recoil velocity is found by integrating the instantaneous momentum flux (found from the Teukolsky equation) over two parts of the history of the binary, the adiabatic inspiral phase (characterized by a slowly shrinking circular orbit) and the non-adiabatic "plunge" phase (dominated by strong-gravity effects) which occurs for separations less than the ISCO (innermost stable circular orbit). FHH extrapolated to the comparable mass regime using scaling functions obtained from post-Newtonian expressions for the momentum flux, first obtained for binaries without spin by Fitchett [13], which are valid for all mass ratios in the inspiral phase. However, the majority of the recoil is due to the plunge. Not knowing the form of the momentum flux in the plunge, but knowing that it must redshift away at the horizon and match a power law form at the innermost stable circular orbit (ISCO), FHH made an assumption for the momentum flux that satisfied both properties. A redshifting condition kept the momentum flux with respect to proper time constant as the separation dropped below 3 times the total mass of the system. The form of the redshift was somewhat arbitrary.

Blanchet, Qusailah, and Will [17] (hereafter BQW) more recently attempted to solve the mass-ratio and plunge problems in the post-Newtonian (PN) approx-

imation, which assumes weak gravity and slow motion but makes no assumption about the mass ratio. They treated only the case of zero black hole spins and found that the recoil velocity could be up to 250 km/s, with apparently less uncertainty than FHH. BQW derived the inspiral momentum flux for non-spinning holes to second post-Newtonian (2PN) order; that is to $O(Gm/rc^2)^2$ beyond leading order, building on the 1PN work of Wiseman [15]. The BQW momentum flux for small separations is qualitatively different from Wiseman's flux, because of the well-known tendency of 1PN calculations to substantially underestimate relativistic effects. BQW introduced a more sophisticated form of the plunge than FHH, subtracting a small amount of energy and possibly angular momentum from the ISCO and integrating the PN momentum flux along the resulting geodesic until the formation of a common horizon. In this treatment the redshifting away of the flux to make the final recoil velocity finite appears more natural than in FHH, but see below.

Although BQW referred to their treatment of the plunge as effective one-body (EOB), it was Damour and Gopakumar [18] who subsequently performed the first truly EOB recoil calculation. The EOB approach includes the effects of finite mass ratio (like PN) and strong gravity (like test-mass perturbation theory). As such, it should give more accurate results than either of the previous approximations although it is limited by the validity of the mapping of the two-body Hamiltonian onto the effective one-body Hamiltonian. Using this approach for non-spinning black holes, Damour and Gopakumar find recoil velocities substantially lower than those of FHH and BQW—probably less than 100 km/s. Most of the discrepancy comes not from the finite mass-ratio effects but from the scaling of the momentum flux during the plunge. Damour and Gopakumar pointed out that the BQW scaling implicitly assumes Kepler's law relation between the frequency and separation, which is not a good assumption in the late stages of the plunge where most of the final recoil velocity is accumulated.

Our contribution in this work is to treat the effects of black hole spins in more detail. Building on the previous work by Kidder [16], we extend the BQW result for the 2PN momentum flux to include the effects of the black hole spins as long as they aligned with the angular momentum of the orbit. This is important for non-extreme mass ratios because the spin contribution to the momentum flux can

exist even for the equal-mass case, where the non-spin terms vanish identically. (Like the other previous work on recoil, we derive the momentum flux assuming no appreciable orbital eccentricity.) Formally speaking we obtain the 1.5PN and 2PN corrections to the leading order spin contribution (0.5PN) to the momentum flux found by Kidder. The adiabatic inspiral phase contribution to the final recoil, including the effects of mass ratio, is easily obtained from the resulting momentum flux.

As in previous work, the plunge is the hard part. Several things which work without spin become difficult or impossible with spin. Approximating the plunge trajectory as a geodesic (neglecting radiation reaction) is justified (for extreme mass ratio) for two reasons. Ori and Thorne [21] have argued that the Kerr potential dominates the dynamics over radiation reaction. Additionally, the corrections due to spin curvature coupling appear at high enough order (2.5PN) that they do not effect the 2PN computation [38, 39]. (There is also an issue of which geodesic to choose, which we address in the Ori-Thorne approximation.) However, the natural vanishing of the proper momentum flux at the horizon, which is a fundamental part of the BQW and Damour-Gopakumar results, does not happen in Kerr. The difference is essentially frame dragging: In Schwarzschild, the angular frequency with respect to coordinate time goes to zero at the horizon; but in Kerr it does not. Thus the final recoil velocity computed from the 2PN momentum flux is sensitive to the behavior of the momentum flux near the horizon. For significant spins, much of the contribution to the recoil comes from near or even within the light ring. On physical grounds we argue that very little should come from within the light ring, and we compare results with the integration terminated at the light ring to those terminated at the horizon.

We use the following notation and conventions: Newton's gravitational constant and the speed of light are set to unity. All tensors are Cartesian, indices may be raised and lowered with the Kronecker delta, and the Einstein summation convention holds even if both indices in a pair are superscripts. A capitalized tensor index means a multiple index—for example, $I^L = I^{abc}$ for $\ell = 3$. A number in parentheses over a tensor indicates repeated differentiation with respect to time—for example, (3) indicates the third time derivative.

2.2 Post-Newtonian expansion

The post-Newtonian expansion is a perturbative method to find analytic solutions to Einstein's Equations [40]. The underlying assumptions of the expansion are the slow motion and weak field (gravity) approximations. The PN expansion has been used to find waveforms for compact binary inspirals accurate enough to use as a tool in LIGO data analysis to identify binary inspiral events. There are currently two popular frameworks for the post-Newtonian expansion. The post-Minkowski formalism was developed by Blanchet *et al.* in [41, 42, 43, 44, 45, 46]. The alternative framework, called the Direct Integration of Relaxed Einstein Equations (DIRE), was developed by Will *et al.* in [47, 48, 15, 49, 50, 51, 52]. This brief introduction will primarily focus upon using the latter formalism to explain the post-Newtonian expansion.

Einstein's equations form a nonlinear system of differential equations given in the form

$$G^{\alpha\beta}[g_{\mu\nu}] = 8\pi T^{\alpha\beta}, \tag{2.1}$$

where $G^{\alpha\beta}$ is the Einstein tensor and $T^{\alpha\beta}$ is the stress-energy tensor. If the gravitational field is weak then one can consider the gravitational waves as a perturbation of the metric on a flat (Minkowski) background metric. This motivates us to define a potential $h^{\alpha\beta}$ as [52]

$$h^{\alpha\beta} \equiv \eta^{\alpha\beta} - (-g)^{1/2} g^{\alpha\beta} \tag{2.2}$$

where g is the determinant of the metric $g^{\alpha\beta}$, and $\eta^{\alpha\beta}$ is the Minkowski metric. We can apply gauge constraints, known as the transverse-traceless gauge, to the potential $h^{\alpha\beta}$. These conditions take the form [53]

$$h^{0i} = 0 \tag{2.3}$$

$$h^{\alpha}_{\alpha} = 0, \tag{2.4}$$

for spatial indices $i = 1, 2, 3$. There still remains enough gauge (or coordinate) freedom to make an additional assumption, namely that

$$\partial_\beta h^{\alpha\beta} = 0 \tag{2.5}$$

which is known as the harmonic gauge condition. Coordinate systems where this gauge condition is satisfied are known as harmonic coordinate systems. Einstein's equations can now be simplified to the point where they now assume the form of a wave equation with a source

$$(-\partial^2/\partial t^2 + \nabla^2)h^{\alpha\beta} = -16\pi\tau^{\alpha\beta}[h^{\alpha\beta}] \tag{2.6}$$

where $\tau^{\alpha\beta}$ is the effective stress-energy pseudo-tensor [54], which is quadratically dependent on $h^{\alpha\beta}$. The effective source $\tau^{\alpha\beta}$ is nonzero even for black holes, where $T^{\alpha\beta}$ vanishes. The set of equations (2.6) is known as the relaxed Einstein's equations. The effective stress-energy tensor $\tau^{\alpha\beta}$ includes the stress-energy tensor $T^{\alpha\beta}$ as well as nonlinear terms in $h^{\alpha\beta}$. The nonlinear contribution to the effective source can be partly understood as gravitation itself contributing as a source for gravitational wave emission. The nonlinear contribution also plays the role of accounting for the effect of treating a curved background as flat.

The defining characteristic of the DIRE framework is obtaining a perturbative solution for $h^{\alpha\beta}$ as the retarded Green's function solution to the relaxed Einstein's equations (2.6)

$$h^{\alpha\beta}(t, \boldsymbol{x}) = 4 \int d^4x' \frac{\tau^{\alpha\beta}(t', \boldsymbol{x'})\delta(t' - t + |\boldsymbol{x} - \boldsymbol{x'}|)}{|\boldsymbol{x} - \boldsymbol{x'}|} \tag{2.7}$$

where integration is done over the past null cone emanating from the field point $(t, \boldsymbol{x})$.

Because gravitation acts as a source, the effective source $\tau^{\alpha\beta}$ has non-compact support at higher order in h. Consequentially, the Green's function integral must be carefully regularized to be evaluated. The DIRE framework and the post-Minkowski framework offer alternative methods to regularize these integrals with non-compact support. Both divide the spacetime into regions where $\tau^{\alpha\beta}$ is dominated by one type of source. The principal regions are the near zone and the far zone, also called the radiation zone. The near zone is a worldtube surrounding the matter or black holes. Within the near zone $T^{\alpha\beta}$ and static fields dominate the effective source. In the far zone, the radiation dominates the effective source. In the DIRE framework the boundary between the two regions is sharp, but semi-

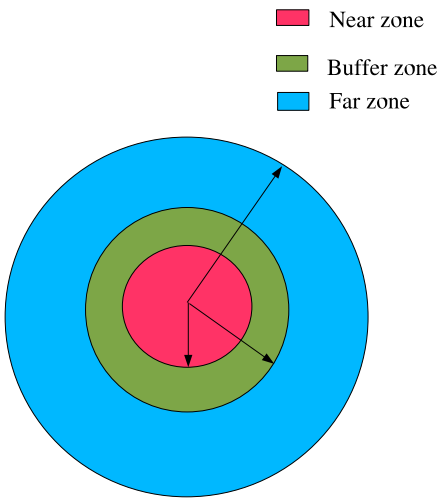

Figure 2.1. Cross-section of the three zones or world tubes

arbitrary. In the post-Minkowski framework the zones are separated by a buffer region where both solutions are asymptotically valid. These three zones are illustrated in figure 2.1. In both methods, the size of the near zone is assumed to be about one characteristic gravitational wavelength.

Applying the weak field $M/r \ll 1$ and the slow motion $v \ll 1$ conditions, we Taylor expand $\tau^{\alpha\beta}$ in powers of M/r and v. These approximations are dependent on each other through a virial type relation $v^2 \sim M/r$. Thus the expansion is, for all intents and purposes, really dependent on only one variable. The Taylor expanded $\tau^{\alpha\beta}$ is used to evaluate the part of the retarded integral where the null cone intersects the near zone. The Taylor expansion of $\tau^{\alpha\beta}$ is identified as the multipole decomposition of $\tau^{\alpha\beta}$. The spatial part of the integral is terminated at the edge of the near zone. The far zone contribution to the integral is computed separately, making use of a coordinate transformation that makes the integral manifestly convergent. The boundary terms from the near zone contribution are canceled by the boundary terms in the far zone contribution, thus making the procedure independent of the choice of the location of the boundary between the near zone and the far zone. Only one solution is found in the DIRE framework, in

$$\begin{array}{c} \tau^{\alpha\beta}_{(0)} \rightarrow h^{\alpha\beta}_{(0)} \\ \swarrow \\ \tau^{\alpha\beta}_{(1)} \rightarrow h^{\alpha\beta}_{(1)} \\ \vdots \end{array}$$

Figure 2.2. The bootstrap process to perturbatively solve Einstein's equations.

contrast with the the post-Minkowski formalism. In the post-Minkowski formalism separate solutions are found for the gravitational field in the near zone and the far zone. The solutions are then matched (using matched asymptotic analysis) in a buffer region where both solutions are assumed to be valid [46].

Assuming that the metric perturbation is small, we treat the nonlinear terms $\mathcal{O}(h^2)$ that appear in (2.6) in a perturbative prescription as follows. The solution to $h^{\alpha\beta}$ is used to find the next order correction to $\tau^{\alpha\beta}$ due to $h^{\alpha\beta}$. Then the next order in $h^{\alpha\beta}$ is solved for using the higher order $\tau^{\alpha\beta}$ that was obtained. The equation of motion is

$$\nabla_\beta T^{\alpha\beta} = 0, \tag{2.8}$$

where ∇ is the covariant derivative that keeps the metric covariantly constant. The equation of motion is used to adjust the harmonic coordinate system and the trajectory of the source. To put it concisely each function is used to find the next order corrections from the other. This method is illustrated schematically in figure 2.2.

2.3 Multipole decomposition

It follows from the general form of the stress-energy tensor that one can calculate the linear momentum flux from the energy flux density by the expression [55]

$$\frac{dP^a}{dt} = \int \frac{d^2E}{d\Omega dt} n^a r^2 d\Omega \tag{2.9}$$

where the integral is over a sphere at infinity and n^a is the unit normal to the sphere. If the energy flux or conversely the waveform is isotropic over the sphere, then there is no linear momentum flux. Therefore, it is by virtue of the anisotropic

pattern of gravitational wave emission that there is linear momentum loss. All compact binary sources have anisotropic wave emission, but not all will have a net linear momentum loss. For example, non-spinning equal mass black hole binaries will have no net linear momentum flux.

The energy flux density can be obtained from either the effective stress-energy pseudo-tensor $\tau^{\alpha\beta}$ or the field $h^{\alpha\beta}$. The gravitational field has a well known radiative multipole decomposition into *pure spin* tensor spherical harmonics. It can be shown that due to the transverse, traceless spin 2 nature of gravitational radiation, the expression of the waveform only depends on the *electric* and *magnetic* tensor spherical harmonics [55] $T^{E2,lm}, T^{B2,lm}$; so called because they obey electric and magnetic type parity with respect to l,

$$\boldsymbol{\pi} T^{E2,lm} = (-1)^l T^{E2,lm}, \tag{2.10}$$

$$\boldsymbol{\pi} T^{B2,lm} = (-1)^{l+1} T^{B2,lm}, \tag{2.11}$$

where $\boldsymbol{\pi}$ is the parity operator. Consequentially, only the mass and current multipoles I^{lm} and J^{lm} associated with those harmonics are needed to characterize the field.

$$h_{jk} = \sum_{l=2}^{\infty} \sum_{m=-l}^{l} \left[\frac{\overset{(l)}{I^{lm}}(t-r)}{r} T^{E2,lm}_{jk} + \frac{\overset{(l)}{J^{lm}}(t-r)}{r} T^{B2,lm}_{jk} \right] \tag{2.12}$$

However it is more convenient to use the symmetric trace-free (STF) multipole moments defined to be Cartesian tensors given by

$$\mathcal{I}_L(t-r) = \frac{l!}{4} \left[\frac{2(l-1)l}{(l+1)(l+2)} \right]^{1/2} \sum_{m=-l}^{l} I^{lm}(t-r) \mathcal{Y}^{lm}_L, \tag{2.13}$$

$$\mathcal{J}_L(t-r) = -\frac{(l+1)!}{8l} \left[\frac{2(l-1)l}{(l+1)(l+2)} \right]^{1/2} \sum_{m=-l}^{l} J^{lm}(t-r) \mathcal{Y}^{lm}_L, \tag{2.14}$$

where $\{\mathcal{Y}^{lm}_L\}$ are rank l tensors defined by satisfying the two properties of generating the scalar spherical harmonics $\{Y^{lm}\}$, and forming a basis for the space of all STF tensors of a given rank l. The capitalized index label L denotes l indices $i_1 i_2 \cdots i_l$. These multipole moments are also known as the mass $\mathcal{I}^L$ and current $\mathcal{J}^L$ multipoles. They are the common definition must used for STF mass and

current multipoles. Radiative multipoles characterize both the material and gravitational aspects of the source, and thus are evaluated from $\tau^{\alpha\beta}$ instead of $T^{\alpha\beta}$. In the post-Minkowski formalism, matched asymptotic analysis uniquely determines these multipoles by matching the near zone multipoles with the far zone multipoles, which are in turn constrained by the no incoming radiation boundary condition.

Now evaluating (2.9) using the known multipole decomposition of the waveform, the linear momentum flux can be shown to have the following multipole decomposition

$$\frac{dP_a}{dt} = \sum_{l=2}^{\infty} \left\{ \frac{2(l+2)(l+3)}{l(l+1)!(2l+3)!!} \langle \overset{(l+2)}{\mathcal{I}}_{aL} \overset{(l+1)}{\mathcal{I}}_{L} \rangle + \frac{8(l+3)}{(l+1)!(2l+3)!!} \langle \overset{(l+2)}{\mathcal{J}}_{aL} \overset{(l+1)}{\mathcal{J}}_{L} \rangle \right. \\ \left. + \frac{8(l+2)}{(l-1)(l+1)!(2l+1)!!} \langle \epsilon_{apq} \overset{(l+1)}{\mathcal{I}}_{p(L-1)} \overset{(l+1)}{\mathcal{J}}_{q(L-1)} \rangle \right\} \quad (2.15)$$

It becomes immediately apparent that purely mass quadrupolar radiation can not produce a linear momentum flux. This is in direct contrast to the energy and angular momentum loss. The linear momentum flux will be evaluated using the post-Newtonian expansion, which involves nonlinear effects unlike electrodynamics.

2.4 Gravitational wave tails

The radiative multipoles, discussed briefly in the previous section, depend on $\tau^{\alpha\beta}$ evaluated at not just at the retarded time, but the entire past history. This is explained by the fact that gravitational waves can scatter off the background curvature of the spacetime [50]. Mathematically this effect is due to the Green's function integration (2.7) being over a null cone on a flat spacetime, when the integration should be over a null cone in the real spacetime, which being curved will produce the scattering effect. This discrepancy between the null cones is resolved by part of the nonlinear contribution to the effective source $\tau^{\alpha\beta}$. The terms end up taking the form of integration over the past history. Thus the mathematics coincides with the physical explanation. Wave tails are the lowest order of the nonlinear phenomena surrounding strong gravitation. Another example of these nonlinear phenomena is the Christodoulou memory [56]. The Christodoulou memory is mathematically explained as high order terms that can be interpreted to be

present due to the fact that gravitational waves themselves radiate. By the equivalence principle, the energy that gravitational waves carry are considered a source, and in that sense are part of the source [49]. It should be noted that memory and other higher order nonlinear effects are not needed for the order at which the computation is outlined in the subsequent sections.

To put it more precisely, both formalisms for the PN expansion automatically account for the tail in their respective methodologies. In the DIRE formalism, the tail contribution arises from the term $h^{00}h^{\alpha\beta}$ in $\tau^{\alpha\beta}$. That term represents modifying the metric by the potential h^{00}, and thus changing the null cones by that scalar factor [51]. Therefore, it is apparent that the difference is interpreted as the difference between the null cones in the actual curved spacetime and the flat background the potential $h^{\alpha\beta}$ is defined on. Although the origin of the tail effects in the post-Minkowski formalism differs significantly from the DIRE formalism, the calculation turns out to be the same.

In the post-Minkowski formalism, because there are two solutions to the metric, one provided in the near zone and another in the far zone, the gauge constraints will also differ between the zones. The implication being that the coordinate systems for either zone will differ from each other. To perform the asymptotic matching of the near zone and far zone multipoles within the buffer region, you need to transform between the near zone harmonic coordinate system [45] and the far zone radiative coordinate system, so that the multipoles are being matched on the same coordinate system. The coordinate transformation needed for the matching has a physical interpretation as accounting for the discrepancy between null cones between the assumed flat background and the actual curved background. And furthermore, the transformation assumes the form of the difference between the radiative and source multipoles are integrals of the source multipoles over the past history. Therefore the two methods mathematically produce the same tail effects with the same interpretation. The nonlinear effects of gravitational radiation is one key complication that arises in the computation outlined in this chapter. The other is the nature of the trajectory itself, even when modeled as a test particle in Kerr.

2.5 Geodesics in Kerr spacetime

To integrate the linear momentum flux, one must model the different phases of the orbit. The plunge phase is modeled as a test particle following an equatorial orbit around a spinning black hole. This model has unusual behavior that does not manifest in the non-spin case. And more realistic orbits that are not explored here are even more challenging to model.

Kerr spacetime is the general solution of Einstein's equations for uncharged axially symmetric stationary spacetimes. There are a few important conceptual ways that the Kerr spacetime differs from the Schwarzschild (spherically symmetric stationary vacuum) spacetime that makes it challenging to use as a model to imitate the plunge orbit of a binary black hole system.

The line element in Kerr given in Boyer-Lindquist coordinates is

$$\begin{aligned} ds^2 &= -\frac{\Delta - a^2 \sin^2\theta}{\rho^2} dt^2 - 2a \frac{2Mr \sin^2\theta}{\rho^2} dt d\phi \\ &+ \frac{(r^2+a^2)^2 - a^2 \Delta \sin^2\theta}{\rho^2} \sin^2\theta d\phi^2 + \frac{\rho^2}{\Delta} dr^2 + \rho^2 d\theta^2 \end{aligned} \tag{2.16}$$

where

$$\Delta \equiv r^2 - 2Mr + a^2 \tag{2.17}$$

$$\rho^2 \equiv r^2 + a^2 \cos^2\theta \tag{2.18}$$

and a and M are the spin and mass parameters of the black hole respectively. Notice that the metric $g_{\mu\nu}$ has an off-diagonal term $g_{\phi t}$. This is not the manifestation of a poor choice of coordinates, but rather an important feature of Kerr spacetime. It is associated with a phenomenon known as frame dragging. Frame dragging is the effect where particles can acquire orbital angular momentum. Particles are dragged to rotate with the black hole.

One of the consequences of frame dragging is that retrograde orbits are unstable further out than the orbits in Schwarzschild. Because of this the innermost stable circular orbit is pushed outwards with increasing $|a|$. And for prograde orbits the opposite occurs; namely the innermost stable circular orbit is pushed inwards with increasing $|a|$. The innermost stable circular orbit (ISCO) for a particle in the

presence of a black hole with extremal spin ($|a| = 1$) is $9M$ for retrograde orbits and M for prograde orbits. That is significantly different from Schwarzschild, where the ISCO is $6M$.

There are two horizons for a Kerr black hole. This contrasts with Schwarzschild, which has only the one horizon. The outer horizon r_+ is the event horizon, the inner horizon r_- is the Cauchy horizon. A particle may fall through the outer horizon and pass into the inner horizon in finite proper time. Not much is physically known about what would happen to the particle once it has fallen inside the inner horizon [53]. The expressions for the horizons are derived from the coordinate singularity in the metric that occurs where $\Delta = 0$ and are

$$r_+ = M + \sqrt{M^2 - a^2} \tag{2.19}$$

$$r_- = M - \sqrt{M^2 - a^2}. \tag{2.20}$$

In addition to the two horizons, there is also a volume called the ergosphere. The ergosphere is defined as the region where $r_+ < r < M + (M^2 - a^2 \cos^2 \theta)^{1/2}$. Within the ergosphere no particle can remain stationary (in the sense that the time translation Killing field is spacelike). This is another nontrivial feature of Kerr geometry that is not present in Schwarzschild geometry.

One important feature common to both is the light ring. Within the light ring, no particles or photons can escape. It is defined as the minimum radius where a circular orbit (either stable or unstable) can exist. Just as there are two horizons, there are two light rings, one for prograde orbits, the other for retrograde orbits, which are given by [57]

$$r_{LR} = 2M \left(1 \mp \cos \left[\frac{2}{3} \arccos \frac{|a|}{M} \right] \right). \tag{2.21}$$

It is then no surprise that the geodesics in Kerr can be different in striking ways from the geodesics in Schwarzschild. When thinking about test particles orbiting a Kerr black hole there are two important ways in which they are different. Highly eccentric orbits close to the black hole whirl around the black hole, but then zoom out to a much larger radius, and orbit there slowly before coming back in [58] as illustrated in figure 2.3. Although this can occur in Schwarzchild black

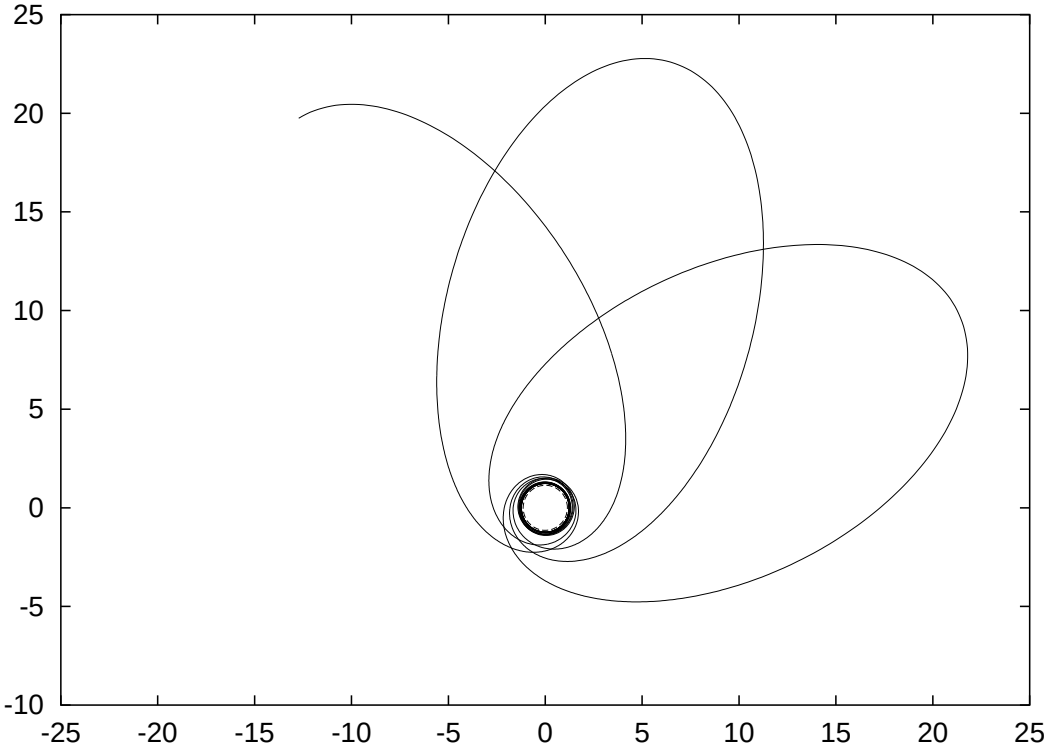

Figure 2.3. Typical zoom-whirl orbit, courtesy Glampedakis and Kennefick [58]

hole systems, eccentricities are more pronounced in Kerr. The other non-trivial behavior of geodesics in Kerr is that of precession. Orbits out of the equatorial plane can precess. This leads to orbits that even without eccentricity fill a sphere up over time. These orbits are called spherical orbits. Spherical orbits exhibit complex behavior. Not only are they not confined to a plane (at least a stationary one), but the points where the orbits intersect the equatorial plane are frame dragged [59]. The plane of the orbit itself precesses. In conclusion, circular equatorial orbits only form a small class of a much larger family of complex orbits that test particles can assume in the presence of a spinning black hole.

2.6 Momentum flux

A binary composed of spinning black holes can be described by the masses (m_1, m_2) and spin 3-vectors $(\mathbf{S}_1, \mathbf{S}_2)$ of the holes as well as the holes' separation r and relative velocity $v = v_1 - v_2$ (we use harmonic coordinates). It is convenient to

reparametrize the masses by $M = m_1 + m_2$, $\eta = m_1 m_2/M^2$, and $\Delta = (m_1 - m_2)/M = -\sqrt{1-4\eta}$ (where the sign is fixed by the arbitrary choice $m_2 \geq m_1$). This is not the same Δ as the one in the previous section. Assuming that both spins are parallel to the angular momentum of the (circular) orbit, we can construct a basis of unit 3-vectors $\mathbf{n}$ (pointing to hole 1 from hole 2), $\boldsymbol{\lambda}$ (parallel to the relative velocity), and $\mathbf{z}$ (parallel to the angular momenta). Then we only need the z-component of each spin, S_1 and S_2. It is convenient to use the spin parameters

$$\chi_\pm = (S_1/m_1^2 \pm S_2/m_2^2)/2 \tag{2.22}$$

of Will and Wiseman [51] because they isolate the antisymmetry of the system which is needed for recoil.

In this case, the momentum flux emitted by the binary is given to 2PN order by

$$\frac{dP^a}{dt} = -\frac{464}{105}\lambda^a X^{11}\eta^2 \sum_{p=0}^{4} F_p X^p \tag{2.23}$$

where $X = (Mv/r)^{1/3}$ is a convenient expansion parameter comparable to the velocity but invariant under a class of gauge transformations. This expression including only the leading order coefficient

$$F_0 = \Delta \tag{2.24}$$

was found by Fitchett [13]. The 1PN coefficient

$$F_2 = \Delta\left(-\frac{452}{87} - \frac{1139}{522}\eta\right) \tag{2.25}$$

was found by Wiseman [15]. The 0.5PN coefficient

$$F_1 = \frac{7}{29}(\chi_- + \Delta\chi_+), \tag{2.26}$$

the leading-order spin effect, was found by Kidder [16]. At higher orders spin and non-spin terms become intermingled. The 1.5PN coefficient contains two contri-

butions $F_3 = F_3^M + F_3^S$, where

$$F_3^M = \frac{309}{58}\pi\Delta \tag{2.27}$$

depends only on the masses of the holes (and is a "tail" term), and

$$F_3^S = \left(-\frac{739}{174} + \frac{1304}{87}\eta\right)\chi_- + \left(-\frac{739}{174} + \frac{322}{87}\eta\right)\Delta\chi_+ \tag{2.28}$$

contains the spin dependence. The 2PN coefficient contains three contributions $F_4 = F_4^M + F_4^S + F_4^{SS}$, where

$$\begin{aligned} F_4^M &= \Delta\left(-\frac{71\,345}{22\,968} + \frac{36\,761}{2088}\eta + \frac{147\,101}{68\,904}\eta^2\right), && (2.29)\\ F_4^S &= \frac{21}{29}\pi(\chi_- + \Delta\chi_+), && (2.30)\\ F_4^{SS} &= \left(-\frac{28}{29} + \frac{54}{29}\eta\right)\chi_-\chi_+ + \left(-\frac{14}{29} - 5\eta\right)\Delta\chi_-^2 \\ &\quad + \left(-\frac{14}{29} + \frac{143}{29}\eta\right)\Delta\chi_+^2 && (2.31) \end{aligned}$$

are mass-only, spin (tail), and spin-spin terms respectively. In F_3 and F_4 the mass-only terms were derived by Blanchet, Qusailah, and Will [17] and the spin-dependent terms are derived for the first time here.

The linear momentum flux due to gravitational wave emission from a post-Newtonian source can be written as a symmetric-trace-free (STF) multipole expansion,

$$\begin{aligned} \frac{dP^a}{dt} &= \sum_{\ell=2}^{\infty}\left[\frac{2(\ell+2)(\ell+3)}{\ell(\ell+1)!(2\ell+3)!!}\,I^{aL}\,I^{(\ell+2)(\ell+1)L}\right. \\ &\quad + \frac{8(\ell+2)\epsilon^{abc}}{(\ell-1)(\ell+1)!(2\ell+1)!!}\,I^{b(L-1)}\,J^{(\ell+1)c(L-1)} \\ &\quad \left. + \frac{8(\ell+3)}{(\ell+1)!(2\ell+3)!!}\,J^{aL}\,J^{(\ell+2)(\ell+1)L}\right], \end{aligned} \tag{2.32}$$

as given for example by Eq. (4.20′) of the review by Thorne [55]. Here I^L and J^L are mass and current multipoles, which can be defined as integrals over the source.

Strictly speaking, Eq. (2.32) should be given in terms of radiative multipoles, which differ from the source multipoles by terms which give rise to physical effects off the light cone such as "tails" and "memory." (For more information on the computation of source and radiative multipoles, see the review by Blanchet [60].) For our purposes it is enough to use the source multipoles given above, with the exception of augmenting the mass and current quadrupoles with tail terms which we shall do explicitly below.

To compute the new terms in Eq. (2.23), only the first few terms in Eq. (2.32) are needed. Kidder's term in Eq. (2.23) is overall of order χv^{12}, where χ here indicates either spin parameter. The new terms in Eq. (2.23) are proportional to χv^{14}, χv^{15}, and $\chi^2 v^{15}$. The mass and current multipoles have low-order behavior

$$\begin{aligned} I^L &\propto Mr^L \left(1 \,\&\, v^2 \&\, \chi v^3\right), \\ J^L &\propto Mr^L v \left(1 \,\&\, \chi v \&\, v^2 \&\, \chi v^3\right). \end{aligned} \tag{2.33}$$

When $\ell + 1$ time derivatives are taken and the virial theorem $M/r \sim v^2$ is used, the scalings in front of I^L and J^L become $v^{\ell+3}$ and $v^{\ell+4}$ respectively. Thus F_1 required the leading-order spin term in J^{ab} and the leading-order mass term in I^{ab}. Our new terms require the $O(v)^2$ corrections to these. They also require the leading-order spin behavior in I^{ab}, I^{abc}, and J^{abc}, the leading-order mass term in J^{abc}, and mass terms including $O(v)^2$ corrections in I^{ab}, I^{abc}, and J^{ab}.

Thus to compute the new spin contributions to F_3 and F_4 we need only

$$\frac{dP^a}{dt} = \frac{16}{45}\epsilon^{abc}\, \overset{(3)}{I}{}^{bd} \overset{(3)}{J}{}^{cd} + \frac{2}{63}\, \overset{(4)}{I}{}^{abc} \overset{(3)}{I}{}^{bc} + \frac{4}{63}\, \overset{(4)}{J}{}^{abc} \overset{(3)}{J}{}^{bc} + \frac{1}{126}\epsilon^{abc}\, \overset{(4)}{I}{}^{bde} \overset{(4)}{J}{}^{cde}, \tag{2.34}$$

where the leading-order spin coefficient F_1 needed only the first term. For non-precessing binaries in circular orbits, the multipoles are given to the needed order by

$$\begin{aligned} I^{ab} &= M\eta r^2 \left\{ \left[1 + \left(-\frac{1}{42} - \frac{13}{14}\eta \right) \frac{M}{r} \right] n^{ab} \right. \\ &+ \left. \left(\frac{11}{21} - \frac{11}{7}\eta \right) v^2 \lambda^{ab} \right. \end{aligned}$$

$$+ \quad \eta\frac{M}{r}v\chi_+\left(\frac{16}{3}n^{ab}+\frac{8}{3}\lambda^{ab}\right)\Bigg\}, \tag{2.35}$$

$$\begin{aligned} I^{abc} &= -M\eta r^3\left\{\Delta\left[\left(1-\eta\frac{M}{r}\right)n^{abc}+(1-2\eta)v^2n^a\lambda^{bc}\right]\right. \\ &- \left.\eta\frac{M}{r}v\left[\left(\frac{3}{2}\chi_- -\frac{15}{2}\Delta\chi_+\right)n^{abc}+3(\chi_- -\Delta\chi_+)n^a\lambda^{bc}\right]\right\}, \end{aligned} \tag{2.36}$$

$$\begin{aligned} J^{ab} &= -M\eta r^2n^az^b\left\{\Delta v\left[1+\left(\frac{67}{28}-\frac{2}{7}\eta\right)\frac{M}{r}\right]\right. \\ &- \left.\frac{M}{r}\left[\frac{3}{2}(\chi_- +\Delta\chi_+)-\eta\left(\frac{29}{7}\chi_- +\frac{34}{7}\Delta\chi_+\right)\frac{M}{r}\right]\right\}, \end{aligned} \tag{2.37}$$

$$J^{abc} = M\eta r^3n^{ab}z^c\left[(1-3\eta)v+4\eta\chi_+\frac{M}{r}\right]. \tag{2.38}$$

The non-spin contributions to these multipoles are found in Eq. (9) of BQW. The spin contributions are given in Eqs. (A5), (4.20), (4.21), and (A6) of Owen, Tagoshi, and Ohashi [61]. Eqs. (A1) and (A3) of the latter article contain typos which do not propagate to Eq. (A5). The highest-order spin term in the current quadrupole of Owen, Tagoshi, and Ohashi [61] contains genuine errors and recently has been corrected by Blanchet, Buonanno, and Faye [62] in their Eq. (5.4).

Equations (2.35)–(2.38) are convenient because it is simple to take time derivatives of the multipoles in this form. The only terms that are time dependent (to the order needed) are

$$\frac{dn^a}{dt}=\omega\lambda^a, \qquad \frac{d\lambda^a}{dt}=-\omega n^a, \tag{2.39}$$

where $\omega = v/r$ is the angular velocity of the orbit. After differentiating we eliminate ω in favor of v, then eliminate v and M/r in favor of the expansion variable $X = (M\omega)^{1/3} = (Mv/r)^{1/3}$, which is boost-invariant and improves the convergence of post-Newtonian expansions for most quantities. To do this we use the substitutions

$$\begin{aligned} v &= X\left\{1-\frac{1}{3}(3-\eta)X^2-\frac{2}{3}\left[\Delta\chi_- +(1+\eta)\chi_+\right]X^3\right. \\ &\left. +\eta\left(\chi_+^2-\chi_-^2\right)X^4\right\}, \end{aligned} \tag{2.40}$$

$$\frac{M}{r} = X^2\left\{1+\frac{1}{3}(3-\eta)X^2+\frac{2}{3}\left[\Delta\chi_- +(1+\eta)\chi_+\right]X^3 \right. \\ \left. -\eta\left(\chi_+^2-\chi_-^2\right)X^4\right\}, \tag{2.41}$$

which are obtained from inverting the standard equation of motion, given for instance by Eq. (F20) of Will and Wiseman [51] (which contains an overall sign error in the spin-spin term). Thus F_3^S and F_4^{SS} are obtained.

Two of the time derivatives must be augmented by tail terms:

$$\overset{(3)}{I}{}^{ab} \rightarrow \overset{(3)}{I}{}^{ab} + 2M\int_{-\infty}^{0} d\tau\, \overset{(5)}{I}{}^{ab}(\tau)\left(\ln\tau + \text{const.}\right), \tag{2.42}$$

$$\overset{(3)}{J}{}^{ab} \rightarrow \overset{(3)}{J}{}^{ab} + 2M\int_{-\infty}^{0} d\tau\, \overset{(5)}{J}{}^{ab}(\tau)\left(\ln\tau + \text{const.}\right), \tag{2.43}$$

where the constants have no effect until higher PN order as discussed in BQW. The only terms that contribute to F_4^S are the tail of the mass-only part of I^{ab} and the tail of the spin part of J^{ab}, both (separately) through the first term in Eq. (2.34). After contracting, the integrals over "scattering delay" τ are performed with the aid of Eq. (14) of BQW, and F_4^S is obtained.

In the test-mass limit ($m_1 \to 0, \eta \to 0, \Delta \to -1$), the momentum flux reduces to

$$\frac{dP^a}{dt} = \frac{464}{105}\eta^2 X^{11}\lambda^a\left\{1+\frac{7}{29}\frac{S_2}{m_2^2}X-\frac{452}{87}X^2 \right. \\ +\left(\frac{739}{174}\frac{S_2}{m_2^2}+\frac{309}{58}\pi\right)X^3+\left[\frac{71\,345}{22\,968} \right. \\ \left.\left.+\frac{21}{29}\pi\frac{S_2}{m_2^2}-\frac{14}{29}\left(\frac{S_2}{m_2^2}\right)^2\right]X^4\right\}. \tag{2.44}$$

For prograde orbits ($S_2 > 0$), the spin terms enhance the momentum flux as expected due to frame dragging. (The overall sign of $\lambda^a dP^a/dt$ is positive because we are computing the momentum emitted by the system rather than the reaction of the system, which has the opposite sign.)

In the limit of equal-mass black holes ($m_1 \to m_2, \Delta \to 0, \eta \to 1/4$) the mo-

mentum flux reduces to

$$\frac{dP^a}{dt} = -\frac{1}{15}\chi_- X^{12}\lambda^a \left[1 - \frac{29}{14}X^2 + \left(3\pi - \frac{29}{14}\chi_+\right) X^3\right] \tag{2.45}$$

rather than vanishing as it does for non-spinning black holes. Physically, the system requires some asymmetry in order to emit linear momentum, and when the masses are equal the asymmetry in the spins χ_- can serve this role. Now the flux is overall proportional to $S_2 - S_1$, which is the expected dependence of a contribution from frame dragging. As in the non-spinning case, the $O(X)^2$ correction reduces the magnitude of the momentum flux by too much, an artifact of the poor accuracy of the 1PN expression for the orbital frequency, and the $O(X)^3$ tail correction brings it back up.

2.7 Recoil velocity

The recoil velocity of the merged black hole is obtained from linear momentum conservation to be

$$v_x + iv_y = -\frac{1}{M}\int_{-\infty}^{+\infty} dt \left|\frac{dP}{dt}\right| e^{i\phi}, \tag{2.46}$$

where ϕ is the orbital phase and we choose the x and y directions so that the recoil velocity at the end of the adiabatic inspiral phase is in the y-direction. In previous work on recoil, the integration over the history of the merger has been divided into up to three distinct phases: inspiral, plunge, and ringdown. We shall assume that it contributes relatively little for spinning holes as well. The first phase is the adiabatic inspiral, which can be treated as a sequence of circular orbits whose radius changes on a timescale much longer than an orbital period. This phase starts at infinite separation (far in the past) and terminates near the ISCO (innermost stable circular orbit). The second phase is the plunge, which lasts from the ISCO until the formation of a common horizon. In the final phase the only source for momentum flux is the ringdown of the quasinormal modes of the final black hole. The ringdown is not addressed in this computation, but was found by Damour and Gopakumar [18] to contribute to the final recoil velocity much less than the

plunge for non-spinning holes.

2.7.1 General remarks

Previous calculations agree that most of the recoil comes from the plunge. The reason why is simple to understand: For circular motion, the integrand of Eq. (2.46) is periodic and the integral vanishes. The only contribution is due to the slowly changing amplitude of the oscillating integrand, corresponding to the radial component of the trajectory. Unfortunately, the plunge is the hardest feature to treat because it involves rapid motion and strong gravity.

Our treatment of the plunge is closest to that of BQW, who used two methods based on the Schwarzschild spacetime. This corresponds to the physical assumption that the black holes have very different masses, or mathematically that $\eta \to 0$. Both methods are based on starting at the ISCO and "tapping" the small hole so that it falls into the large hole along a similar geodesic. That is, some energy and angular momentum are subtracted from the ISCO to produce a new geodesic which enters the horizon of the large hole. This produces a physically motivated "redshifting away" of the momentum flux which improves on the redshift of FHH. FHH assumed that $|dP^a/d\tau|$ went to a fixed (and somewhat arbitrary) nonzero value near the horizon, where τ is the proper time. BQW have $|dP^a/d\tau|$ tending toward zero at the horizon due to the form of the PN momentum flux and the properties of Schwarzschild geodesics. In BQW's method 2, the energy and angular momentum of the plunge relative to the ISCO were determined by subtracting numbers equivalent to the energy and angular momentum fluxes at the ISCO multiplied by an arbitrary number of ISCO orbital periods. In principle this looks bad because there is a new arbitrary parameter, but BQW found that the final recoil velocity was fairly insensitive to the value of this parameter as long as it was chosen in the range about 0.01–1. Method 1 of BQW attempted to be more physical by keeping the angular momentum of the plunge the same as at the ISCO, but adding the (small) PN radial motion dr/dt to find the plunge geodesic. The final recoil velocity agreed with that of method 2 well, typically within a few percent.

Damour and Gopakumar [18] changed the BQW treatment of the plunge partly

by finite η effects, but mainly by arguing for a different scaling of the momentum flux which does not depend on the existence of a Kepler-like relation between frequency and radius. Simple differentiation of the lowest-order multipoles in (2.34) argues that the momentum flux should scale as $\omega^7 r^5 M^2 \eta^2$ since the mass multipoles scale as $M\eta r^\ell$ and, even in the plunge, angular motion dominates the radial motion so that time derivatives are replaced by powers of ω. Since without spin ω is proportional to the separation from the horizon for small separations from the horizon, this makes the momentum flux with respect to proper time drop as the sixth power of a small quantity instead of the 8/3 power. Using that scaling we reproduce roughly the same numbers as DG, suggesting that the scaling was the important difference between the BQW result and the DG result.

We first tried the BQW methods and found additional difficulties with the inclusion of spin. The dependence of method 2 on the arbitrary "tap" parameter is a much bigger problem for Kerr than for Schwarzschild, and we found it basically useless for significant spins. It is easy to come up with negative energies, for instance. Method 1 can also have negative energies for significant spins, and has conceptual problems. The PN expression for dr/dt is obtained by dividing the energy flux dE/dt by the radial derivative of the energy $E(r)$ of a circular orbit in Newtonian gravity. However, Newtonian gravity has no ISCO. Therefore using it at the ISCO may be suspect, particularly since for prograde orbits the ISCO is located deep within the strong gravity region. Also, retrograde geodesics with energy and angular momentum less than at ISCO typically do not extend out to the ISCO and some means must be found for closing the gap between the ISCO and the plunge geodesic.

We use a method 3 based on an approximation to the transition between inspiral and plunge due to Ori and Thorne [21]. As Ori and Thorne note in their Conclusion, their work was done in the extreme mass ratio limit for Kerr, but for zero spin reduced to the same transition equation of motion as the then-new EOB approach in the limit of extreme mass ratio. Their treatment of the transition phase was in terms of perturbation around the ISCO, Taylor expanding the effective potential to lowest significant order. After scaling to natural units, this results in a universal equation of motion which smoothly joins the adiabatic inspiral to the plunge geodesic. The Ori-Thorne "tap" has a simple physical interpretation: The

energy and angular momentum deficits of the final plunge geodesic are given by the fluxes with respect to proper time multiplied by the duration of the transition in proper time. This is because the fluxes are approximated during the transition by their ISCO values, and during the plunge by zero (implying geodesic motion).

We also ignore the ringdown, which Damour and Gopakumar [18] found to be a small contribution, although with spin it may not be as small.

2.7.2 Our calculation

The adiabatic inspiral phase of binary black hole coalescence is modeled as a sequence of circular orbits, terminating at the ISCO. For generic mass ratios the location of the ISCO is not known (different approximation methods disagree), and thus here we will use the ISCO of a test particle in the Kerr spacetime regardless of mass ratio as BQW did for Schwarzschild. The integration over this phase of the orbit simply uses Eq. (2.39) since radiation reaction effects are higher order corrections, and thus we integrate Eq. (2.46) to obtain

$$v_y = \frac{464}{105}\eta^2 X^8 \sum_{p=0}^{4} F_p X^p \tag{2.47}$$

with X evaluated at the ISCO for the total contribution from the inspiral phase. The extreme mass-ratio approximation enters this part of the calculation only through the location of the ISCO. In table 2.1 we give values of the recoil velocity at ISCO for different values of η and the EOB spin parameters a and s described below.

Recoil velocity (using BQW scaling) at ISCO in km/s as a function of a and η for $s = s_{\rm min}$ and $s = s_{\rm max}$ (which are themselves functions of a and η see Eqns. (2.52), (2.53) ahead). The $a = s = 0$ case agrees with BQW. The ISCO recoil increases with a due to the drawing in of the ISCO. The momentum flux spin parameter s has little effect for small η, but for η large and not 0.25 the recoil is enhanced for low s and reduced for high s. Note that with spins the recoil velocity does not in general vanish as $\eta \to 1/4$. The highest recoil (high a, $s = s_{\rm min}$) corresponds to counter-aligned spins with the orbital angular momentum aligned with the spin of the more massive black hole.

Table 2.1. Recoil velocity (using BQW and DG scaling) at ISCO in km/s as a function of a and η for $s = s_{\rm min}$ and $s = s_{\rm max}$ (which are themselves functions of a and η). The $a = s = 0$ case agrees with BQW and DG respectively. The ISCO recoil for both scalings can be explained due to the drawing in of the ISCO. BQW scaling goes up because X goes up. On the other hand, DG scaling goes down as a is increased due to the y^{-5} damping factor. The momentum flux spin parameter s has little effect for small η, but for η large and not 0.25 the recoil is enhanced for low s and reduced for high s. Note that with spins the recoil velocity does not in general vanish as $\eta \to 1/4$. The highest recoil (high a, $s = s_{\rm min}$) corresponds to counter-aligned spins, with the orbital angular momentum aligned with the spin of the more massive black hole.

	η							
a	0.05	0.10	0.15	0.20	0.24	0.25	s	scaling
0.0	2.7	9.5	17.6	22.2	14.4	0.0	0	BQW
0.0	2.7	9.5	17.6	22.2	14.4	0.0	0	DG
-0.8	1.8	6.4	11.9	15.3	11.4	5.4	min	BQW
-0.8	9.0	31.7	59.2	75.9	50.7	2.7	min	DG
0.0	2.8	9.9	18.9	25.7	21.1	8.2	min	BQW
0.0	2.8	9.7	18.4	24.6	19.9	8.2	min	DG
+0.8	7.9	28.5	55.5	77.3	65.4	25.5	min	BQW
+0.8	0.6	2.0	3.6	4.5	3.0	0.1	min	DG
-0.8	1.8	6.0	10.4	11.7	4.5	5.4	max	BQW
-0.8	0.6	1.9	3.5	4.4	2.8	0.1	max	DG
0.0	2.7	9.1	15.9	18.0	6.9	8.2	max	BQW
0.0	2.7	9.3	16.6	19.5	8.4	8.2	max	DG
+0.8	7.9	28.0	52.6	66.7	36.7	25.5	max	BQW
+0.8	0.6	1.9	3.5	4.4	2.8	0.1	max	DG

Now we change to Kerr and, while we do not use a true EOB treatment with η-dependent effects on the trajectory, we do use the mapping of parameters. The total mass M maps onto the Kerr mass, also written M. We remove the dimensions from all dimensioned quantities (such as a and r) by appropriate powers of M, except the orbital energy E which is normalized by $M\eta$ and the angular momentum L which is normalized by $M^2\eta$. The relationship between the Kerr spin parameter a and the spins of the two black holes is given by Damour [63] as

$$a = \Delta\chi_- + \left(1 - \frac{\eta}{2}\right)\chi_+. \tag{2.48}$$

To finish reparameterizing the two spins we define a second spin parameter

$$s = \chi_- + \Delta\chi_+ \tag{2.49}$$

which captures the leading-order behavior of the spin part of the momentum flux. The PN spin parameters are expressed in terms of these new ones by

$$\chi_+ = \frac{2}{7\eta}(a - \Delta s) \tag{2.50}$$

$$\chi_- = \frac{2}{7\eta}\left[\left(1 - \frac{\eta}{2}\right)s - \Delta a\right]. \tag{2.51}$$

The fact that $|\boldsymbol{S_1}|/m_1^2$ and $|\boldsymbol{S_2}|/m_2^2$ are bounded above by unity translates into bounds on a and s. For equal masses ($\eta = 1/4$), the maximum $|a|$ is 7/8. This is explained in a physically intuitive way by Damour [63]. Here we simply limit our values of $|a|$ to 7/8 or less. Although we could go higher for extreme mass ratio, it is our belief that our approximations are unreliable by then anyway. More important for the display of our results is the effect on the allowable range of s. Setting $|\boldsymbol{S_1}|/m_1^2 = 1$ (a quadratic equation in s) leads to the condition

$$s_{+\pm} = \left[a(\Delta - 1) \pm \frac{7}{2}\eta\right] / \left(1 - \Delta - \frac{\eta}{2}\right) \tag{2.52}$$

while doing the same for $|\boldsymbol{S_2}|/m_2^2$ implies

$$s_{-\pm} = \left[a(\Delta + 1) \pm \frac{7}{2}\eta\right] / \left(1 + \Delta - \frac{\eta}{2}\right). \tag{2.53}$$

Allowing for both possible signs of a (recall $\Delta < 0$), the lower limit $s_{\min}$ is set by $\max(\min(s_{+\pm}), \min(s_{-\pm}))$ and the upper limit $s_{\max}$ is set by $\min(\max(s_{+\pm}), \max(s_{-\pm}))$. (Note that $s = 0$ is not possible for all a and η.)

In Boyer-Lindquist coordinates, the equations for an equatorial (but not necessarily circular) geodesic of energy per unit mass E and angular momentum per unit mass^2 L are given by Chandrasekhar [57] as

$$\frac{dt}{d\tau} = \frac{(1 + a^2y^2 + 2a^2y^3)\,E - 2ay^3L}{1 - 2y + a^2y^2}, \tag{2.54}$$

$$\frac{d\phi}{d\tau} = y^2 \frac{(1-2y)L + 2ayE}{1-2y+a^2y^2}, \tag{2.55}$$

$$y^{-4}\left(\frac{dy}{d\tau}\right)^2 = E^2 + 2(L-aE)^2y^3 - \left(L^2 - a^2E^2\right)y^2 - \left(1-2y+a^2y^2\right) \equiv A(y)^{-2}, \tag{2.56}$$

where τ is the proper time and $y = 1/r$. [Compare Eqs. (69), (70), and (104) of Chandrasekhar's Chapter 7.] Equations (2.54) and (2.55) can be combined with the definition $\omega \equiv d\phi/dt$ to write the PN expansion parameter as

$$X(y) = \left\{ y^2 \left[\frac{(1-2y)L + 2ayE}{(1+a^2y^2+2a^2y^3)\,E - 2ay^3L} \right] \right\}^{1/3}. \tag{2.57}$$

It is straightforward to substitute this expression into Eq. (2.23) to obtain the momentum flux as a function of y. Since all quantities are being expressed as functions of y, it behooves us to change variables to integrate the momentum flux over y instead of the coordinate time t. Combining Eqs. (2.54) and (2.56) yields

$$dt = \frac{1}{y^2}\left[\frac{(1+a^2y^2+2a^2y^3)\,E - 2ay^3L}{1-2y+a^2y^2} \right] A(y)\,dy. \tag{2.58}$$

In Eq. (2.46) we will also obtain the orbital phase by integrating

$$\frac{d\phi}{dy} = \left[\frac{(1-2y)L + 2ayE}{1-2y+a^2y^2} \right] A(y), \tag{2.59}$$

which is obtained by combining Eqs. (2.55) and (2.56).

We also need the values of y at the ISCO (y_0) and at the horizon (y_h), which are given by [57]

$$0 = 3a^2y_0^2 + 6y_0 - 8ay_0^{3/2} - 1, \tag{2.60}$$

$$y_h = 1/(1+\sqrt{1-a^2}). \tag{2.61}$$

From Chandrasekhar [57] Eqs. (116), (117), and (118) we obtain the energy and

angular momentum at the ISCO,

$$E_0 = \frac{1-2y_0+ay_0^{3/2}}{\left(1-3y_0-2ay_0^{3/2}\right)^{1/2}}, \tag{2.62}$$

$$L_0 = \frac{1-2ay_0^{3/2}+a^2y_0^2}{\left[y_0\left(1-3y_0-2ay_0^{3/2}\right)\right]^{1/2}}. \tag{2.63}$$

In method 3 the energy and angular momentum of the final geodesic are given by [21]

$$E' = E_0 - X(y_0)^3(\eta\kappa)^{4/5}(\alpha\beta)^{-1/5}T_{\rm pl}, \tag{2.64}$$

$$L' = E_0 - (\eta\kappa)^{4/5}(\alpha\beta)^{-1/5}T_{\rm pl}. \tag{2.65}$$

The parameters κ, α, and β are scale factors obtained respectively from the energy flux at the ISCO and from partial derivatives of the Kerr effective potential at the ISCO. Their explicit form is

$$\kappa = \frac{32}{5}X(y_0)^7\frac{1+ay_0^{3/2}}{\left(1-3y_0+2ay_0^{3/2}\right)^{1/2}}, \tag{2.66}$$

$$\alpha = 3y_0^4\left\{10(L-aE)^2y_0^2+2a^2\left[\left(E^2-1\right)-L^2\right]y_0+1\right\}, \tag{2.67}$$

$$\beta = 2y_0^3\left[-3(L-aE)\left(1-aX(y_0)^3\right)y_0+L-a^2EX(y_0)^3\right]. \tag{2.68}$$

The quantity $T_{\rm pl}\approx 0.3412$ is the duration of the transition from ISCO to plunge in terms of an appropriately rescaled proper time.

With spin, we cannot always simply use the final geodesic for the plunge as worked without spin. For retrograde orbits, the plunge geodesics are located wholly inside the ISCO—sometimes far inside—and thus we need to consider the transition between ISCO and plunge. At this point it is worth digressing to note the properties we require of the integrand $(dP/dt)(dt/dy)$. No jumps in radius are allowed because dt/dy must be finite (and indeed continuous) apart from the co-

ordinate divergence approaching the horizon. For the recoil the orbital phase is important because the momentum flux has a direction. Thus ϕ must evolve continuously, and indeed $d\phi/dt$ and thus X must be continuous to avoid unphysical jumps in the integrand.

The Ori-Thorne transition equation of motion works out to be

$$\frac{dt}{dy} = -\frac{1}{y_0^2}\frac{dt}{d\tau}\bigg|_{y_0} (\eta\beta\kappa)^{-3/5}\alpha^{2/5}T'(Y(y)), \tag{2.69}$$

where

$$Y(y) = (\eta\beta\kappa)^{-2/5}\alpha^{3/5}\left(\frac{1}{y} - \frac{1}{y_0}\right) \tag{2.70}$$

is the rescaled distance from ISCO (which they write as X). The function $T(Y)$ is found by inverting the (numerically obtained) solution to their universal equation of motion

$$Y''(T) = -Y^2 - T \tag{2.71}$$

which they plot in their last two figures. We use this radial equation of motion, with the angular equation of motion such that $X = \omega^{1/3}$ is held at its ISCO value, from the ISCO inward to the final plunge geodesic for retrograde orbits. We pick up the geodesic version of X again at the point where X returns to its ISCO value. Because the transition dt/dy and the geodesic dt/dy curves do not always intersect (typically missing by 20%), we merge them with a weighted sum that smoothly goes from purely transition at the outermost point of the geodesic to purely geodesic at the horizon. The exact form of this function does not greatly affect the final recoil.

This lack of intersection is a reflection of the limitation of the Ori-Thorne approximation to the case $\eta \to 0$. In general, for η greater than about 0.05 the Ori-Thorne transition extends into the horizon. Thus the energy and momentum loss from ISCO are overestimated. The true plunge is likely to go into the horizon less abruptly, thereby resulting in less final recoil.

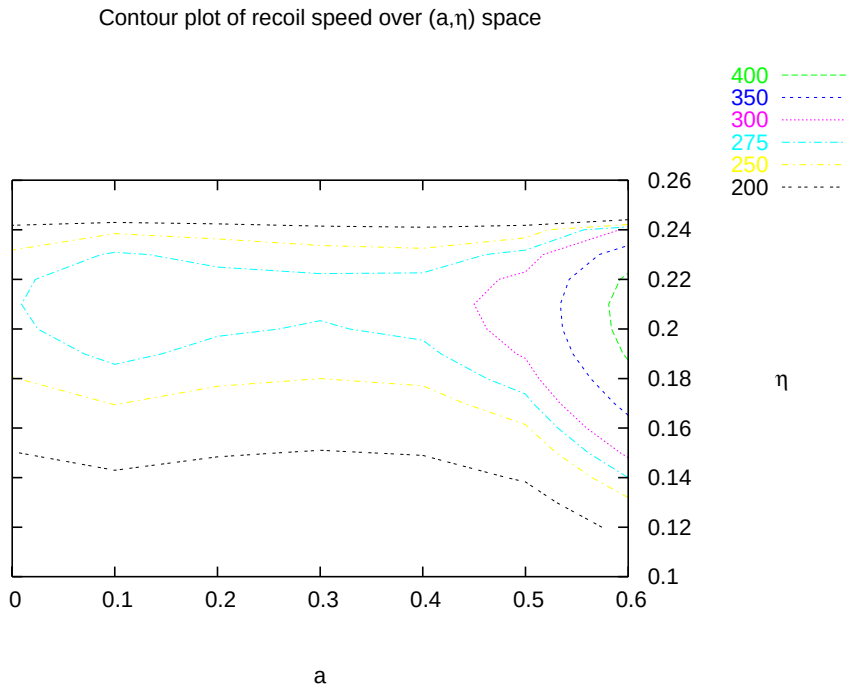

Figure 2.4. Recoil speed using BQW scaling where $s = s_{min}(\eta, a)$. The speeds are significantly large, attaining values up to 1000 km/s. Spin enhances the kick using BQW scaling.

2.7.3 Results

The final recoil velocity is computed using BQW scaling and DG scaling in figures (2.4,2.5) maximizing over s. The values for no spin approximately reproduce the results of BQW and DG respectively, in spite of using different either a different geodesic or an altogether different method.

Investigation of the integrands shows that dt/dy is blowing up and the momentum flux (through X) has its zero moving away from the horizon—in for prograde, out for retrograde—so that it no longer compensates for the dt/dy divergence as it did in Schwarzschild.

In Fig. 2.6 the integrand is plotted for the case $a = s = 0$, similar to BQW. As soon as we move to even modest $a = 0.2$, in Fig. 2.7, we see an apparent dramatic rise which however does not contribute much to the recoil integral (2.46). In fact there dt/dy and $d\phi/dy$ are both diverging, as both the t and ϕ Boyer-

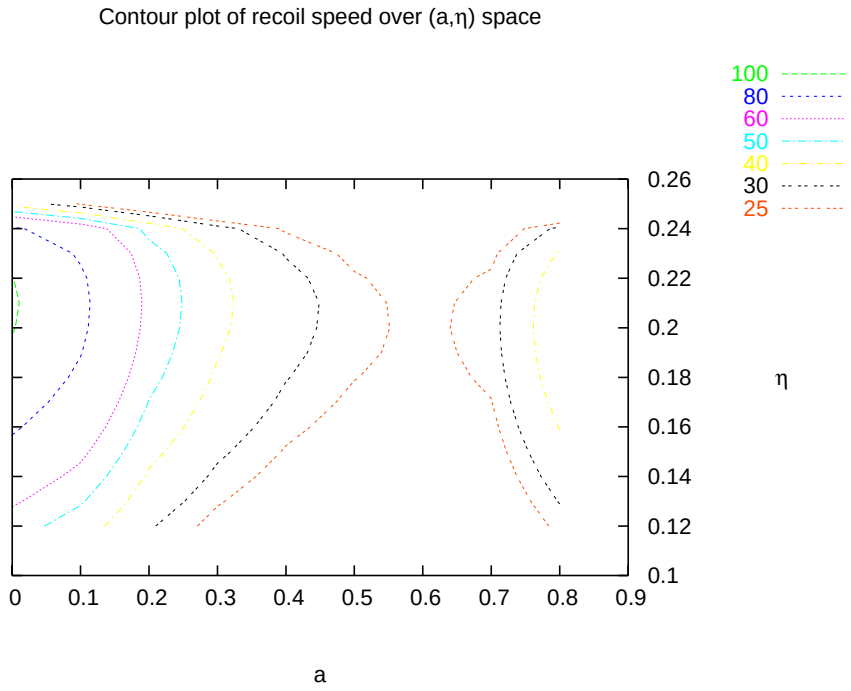

Figure 2.5. Recoil speed using DG scaling where $s = s_{min}(\eta, a)$. The speeds are significantly smaller than BQW scaling. Spin reduces the kick, contrasting with the BQW scaling.

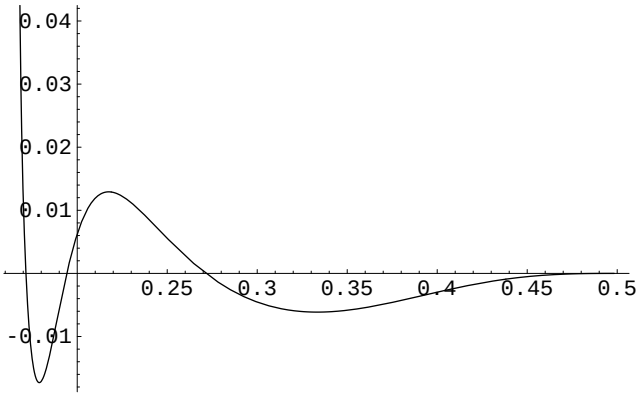

Figure 2.6. Integrand dP_x/dy vs. y for non-spinning black holes ($a = s = 0$). It is clearly well behaved toward the horizon $y_h = 0.5$. It looks similar for different values of s.

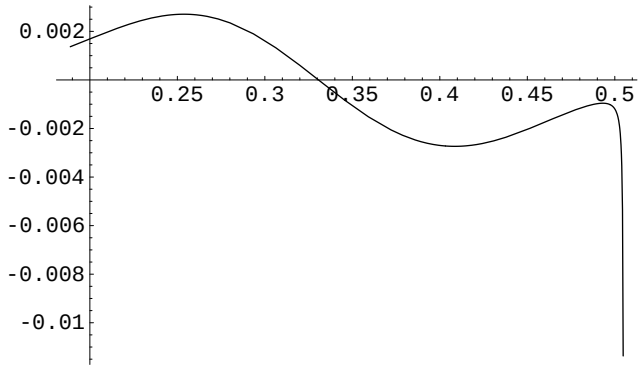

Figure 2.7. Integrand dP_x/dy vs. y for $a = 0.2$ and $s = s_{\min}$. The spike near the horizon contributes less than 1% to the total recoil, in spite of appearances.

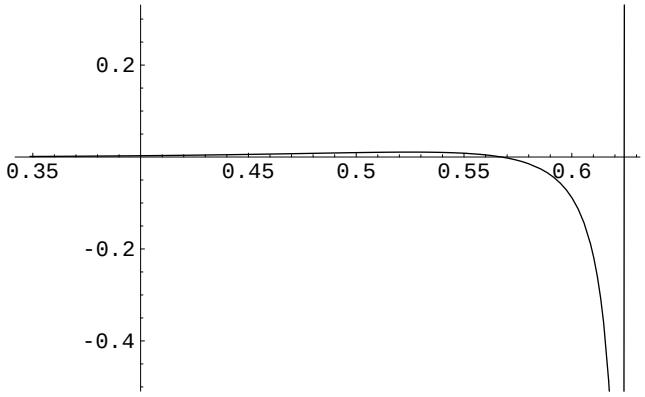

Figure 2.8. Integrand dP_x/dy vs. y for $a = 0.8$ and $s = s_{\min}$. Most of the contribution comes from within the light ring ($y > .55$).

Lindquist coordinates are subject to coordinate singularities near the horizon. This actually makes it possible to evaluate this part of the integral analytically under the assumption that dP/dy changes slowly with respect to the very rapid oscillations of $e^{i\phi(y)}$. This can be shown by taking the limit $y_h - y = \delta y \to 0$ of the geodesic equations. Note that $dt/dy \propto \delta y^{-1}$ for Kerr near the horizon while $d\phi/dt$ tends to a constant. This is in contrast to Schwarzschild where $d\phi/dt \propto \delta y$ near the horizon, and thus $dP/dy \propto \delta y^{8/3}$ which was clearly integrable down to $\delta y = 0$. The integral for Kerr is convergent too, provided the proper momentum flux tends to zero near the horizon as one would expect. Formally $d\phi/dy \propto \delta y^{-1}$, meaning that $\phi(y)$ diverges as $\ln(\delta y)$. Then the final part of the plunge integral is of the form $\int d\ln(\delta y) e^{i\ln(\delta y)}$ times a function which decreases slowly with $\ln(\delta y)$. Provided the

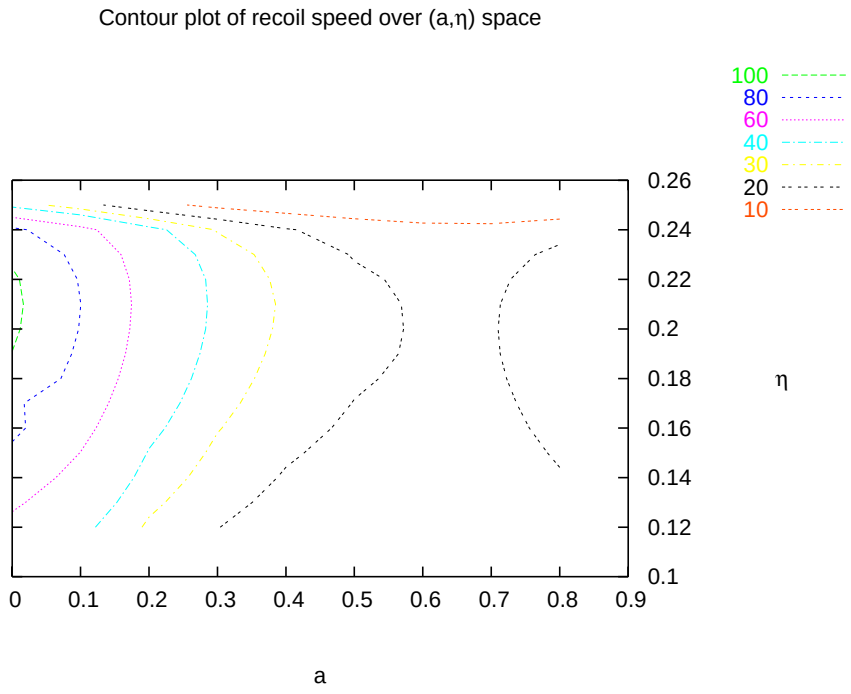

Figure 2.9. Recoil speed using DG scaling and terminating integration at the light ring, instead of the horizon. In contrast to Figure 2.5 the rise in recoil speed is "postponed" to higher values of a, at which other parts of our calculation are becoming suspect anyway.

function decreases slowly, this evaluates the same as the adiabatic inspiral with the antiderivative evaluated at some small δy_c. It can be verified numerically that the choice of δy_c can be varied considerably with negligible change in the final recoil velocity.

The exception is for a strongly positive or negative. Here, as seen in Fig. 2.8, there is a substantial contribution from within the light ring before the last oscillating piece begins. On physical grounds, most of the radiation should be trapped within the light ring, greatly reducing the final recoil velocity for high a, as illustrated in Fig. 2.9.

2.8 Conclusions

Overall spin has the affect of moderately reducing recoil for moderately prograde orbits, with final speeds bounded by 100 km/s, enough for ejection from most globular clusters and dwarf galaxies. If instead of scaling the linear momentum flux by the orbital angular velocity ω as done by Damour and Gopukar [18], we use the boost invariant angular velocity X we would obtain final speeds that can attain values as high as 1000 km/s, with spin greatly enhancing the recoil speeds for prograde orbits. However, the DG scaling is both physically and mathematically well motivated. The bound on the recoil speeds, neglecting the effect of quasinormal mode ringing, should be 100 km/s, with spin having the effect of reducing the recoil speed.

Tools are becoming available to carry this calculation further. Two papers have been recently submitted by Faye, Blanchet, and Buonanno [64, 62]. The first [64] derives the 2.5PN spin terms in the equation of motion, confirming the results of Tagoshi, Ohashi, and Owen [39]. The second [62] computes the 2.5PN energy flux and orbital phase, including a calculation of the spin contributions to the multipoles which expands on the work of Owen, Tagoshi, and Ohashi [61] and corrects a mistake in the renormalization of their post-Newtonian corrections. These ingredients could be combined to obtain the 2.5PN spin contribution to the momentum flux.

However it is debatable how well any PN expansion to the momentum flux will do. It seems that the highest recoil is dominated by the way the momentum flux with respect to proper time vanishes toward the horizon. This is evidenced by the fact that Damour and Gopakumar find a substantially different recoil from BQW when the main difference is effectively the power law with which their flux vanishes.

Integrating the linear momentum flux using the Teukolsky equation without using a Fourier decomposition might provide more realistic dynamics. There is some evidence from the numbers Finn provided for Ori and Thorne [21] that the energy flux decreases steeply toward the horizon (at least for high a), which means the momentum flux would too. That would make the recoil numbers smaller.

Chapter 3

Information Matrix for the LIGO Periodic Sources Search

The LIGO unknown pulsar search is done using the method of maximum likelihood. The log-likelihood function for the pulsar search (after some reduction of the parameter space) is called the F-statistic. From the F-statistic, the Fisher information matrix can be derived, and thus the geometry of the parameter space. An analytic model, which assumes a circular Earth, a circular orbit and neglects amplitude modulation of the signal, is used to determine the geometry of the parameter space. From that an efficient method to tile the parameter space is determined. The Earth's orbit is close enough to being circular that the method is efficient and accurate. It has been implemented for the expensive LIGO pulsar searches under the Einstein@Home distributed computing project.

3.1 The Method of Maximum Likelihood

The Method of Maximum Likelihood [65] is used for parameter estimation when there are analytic models to use for posterior probability distributions. We treat parameters separately from random variables so that the probability density function (pdf) $p(\boldsymbol{x};\boldsymbol{\lambda})$ of M random variables $\boldsymbol{x}$, and N parameters $\boldsymbol{\lambda}$ is defined in the usual way

$$dP = p(\boldsymbol{x};\boldsymbol{\lambda})d^M x \tag{3.1}$$

Then the *likelihood ratio* Q is defined to be the factor of how much more probable one set of parameters is from another. That is one set of values for the parameters, $\boldsymbol{\lambda} = \boldsymbol{\lambda_1}$, is Q times more probable than the other, $\boldsymbol{\lambda} = \boldsymbol{\lambda_1}$ by the ratio

$$Q \equiv p(\boldsymbol{x}; \boldsymbol{\lambda_1})/p(\boldsymbol{x}; \boldsymbol{\lambda_2}). \tag{3.2}$$

So we will now reinterpret $p(\boldsymbol{x}; \boldsymbol{\lambda})$ as a function of the sample, and thus a random variable, which we will call the *likelihood function* L.

Now it becomes clear that parameter estimation should be done by finding the maximum of the likelihood, $\boldsymbol{\lambda} = \hat{\boldsymbol{\lambda}}$. That is

$$\frac{\partial L}{\partial \lambda_\mu} = 0, \tag{3.3}$$

$$\frac{\partial^2 L}{\partial \lambda_\mu^2} < 0, \tag{3.4}$$

for all $\mu = 0, 1, ...N - 1$. However, that is not the practical way that it is usually done.

The pdf is a product of the pdf's for each independent random variable, so one will expect that computing the derivative of the likelihood to be complicated if there are many random variables. However there is an alternative function that will attain a maximum for the same parameters that maximize the likelihood, but is easier to maximize. The logarithm is a monotonically increasing function. So a function is maximum if and only if the logarithm of the function is maximum. Since the log of a product is the sum of logs, it is then both computationally easier and equivalent to maximize the logarithm of the likelihood instead. So we define the logarithm of the likelihood to be

$$l \equiv \ln L \tag{3.5}$$

and the method of maximum likelihood becomes estimating the parameters by finding where the log-likelihood is maximum

$$\frac{\partial l}{\partial \lambda_\mu} = 0, \tag{3.6}$$

$$\frac{\partial^2 l}{\partial \lambda_\mu^2} < 0. \tag{3.7}$$

The Method of Maximum Likelihood is used in several of the pulsar searches, where the likelihood is given by an expression called the F-statistic.

3.2 The F-statistic

There are two important general ways to distinguish between periodic signals that are astrophysical in nature and those that are noise. One method to identify false signals is to use coincidences between multiple interferometers. Gravitational waves are expected to be incident upon all of the detectors. If a suspected signal is not apparent upon all of the detectors, it should be rejected. The other way in which we can distinguish astrophysical sources from terrestrial or instrumental noise is to note that astrophysical sources will be Doppler and phase modulated owing to the motion of the Earth about its axis and about the sun. The Doppler modulation is due to the fact that we are in a non-inertial frame. Because the Earth rotates and orbits the sun, we are continuously accelerating. The pulsars would be perceived as stationary (or steadily moving, with a stationary frequency) in a barycentric frame, but appear to be in motion in our frame. Therefore the periodic sources are not purely monochromatic, but instead are weakly modulated. The method of maximum likelihood can be applied to search for and identify Doppler modulated periodic sources in LIGO data. For this method to be truly effective, the data must be observed over long periods of time. This is the essential concept behind how to search for periodic sources.

The first place to begin on the methodology behind searching the parameter space is defining a detection statistic. We must define a measure of how close the actual signal is to a predicted form or template. There are many such templates that would generically describe the Doppler modulation, but specifically differ from each other in parameter values. The measure or statistic will be the likelihood, giving us a means to determine how to maximize over a family of templates. In

general it is related to the signal-to-noise, which is defined by

$$\rho^2 \equiv 4\Re \int_0^\infty df \frac{\widetilde{u^*}\,(f)\,\widetilde{h}\,(f)}{S_h(f)}, \tag{3.8}$$

where S_h is the power spectral density of the detector noise, h is the data, and u is a template waveform here assumed to be normalized (see ahead). For pulsars there is also the F-statistic [66], which is more complicated but qualitatively similar. The inverse of the power spectral density is used as the weight to account for spectral disturbances in the noise artificially enhancing the statistic. The statistic should be large if the signal h is close to being u. A threshold is set by the analyst, whereby the statistic has to exceed that threshold to be considered an event. A true signal should then trigger events by that thresholding across a small, connected region of the parameter space. Noise or false signals would be expected to trigger templates across many separate regions of the parameter space, because noise does not assume the form of the Doppler modulated template. Matched filtering for pulsars uses a more complicated form of the signal-to-noise (3.8) known as the F-statistic [66].

The F-statistic can be identified as assuming the form of a weighted inner product defined on a continuous function space. Since the detector output is really a vector, we have good reason to identify both signal and templates as vectors. This makes identifying the F-statistic as the inner product between the signal and the template sensible. We will adopt the bra-ket terminology, and we then identify the F-statistic as the signal-to-noise (3.8)

$$\rho^2 = \langle u|h\rangle, \tag{3.9}$$

maximized over the extrinsic parameters (see ahead).

A continuous parameter space can only be searched with a finite number of templates. A discrete grid is chosen to represent the parameter space. The computational cost of searching over the parameter space will be prohibitively expensive if too many templates are used. However, if too few templates are used, there is a risk of losing a signal because it matches with a point in the parameter space that is *too far* from the nearest points on the grid chosen. A way to quantify the separation between templates is needed to identify the optimal way to grid the

parameter space. The inner product defined above can also be used to define a distance function on the space.

$$d(a,b) \equiv \langle u(a)|u(b)\rangle, \tag{3.10}$$

for all points a, b on the parameter space. This is also known as the match between templates when maximized over *extrinsic* parameters [67]. It can then be shown that the metric for the *full* parameter space (using the signal-to-noise) must be

$$\Gamma_{\mu\nu}(\lambda^\alpha) = \langle \partial_\mu u(\lambda^\alpha)|\partial_\nu u(\lambda^\alpha)\rangle, \tag{3.11}$$

for any coordinate λ^α on the parameter space. This is the Fisher information matrix. A search metric defined on the *intrinsic* parameter space, derived from the F-statistic, can also be derived from the information matrix. The geometry of the parameter space provides the necessary knowledge of how to tile the space in such a way that neighboring templates are equally separate. Thus the loss in signal-to-noise due to the discreteness of the grid is uniform, and can then be controlled by one parameter that quantifies the loss in signal-to-noise. This parameter is called the minimal match [67]. For instance, more points should be used in regions where the match falls off quickly, fewer points where the match falls off slowly. One can also imagine that the match between neighboring templates falls off anisotropically, meaning that tiling should be denser proceeding in one direction than another. In conclusion, the tiling is determined ultimately from the information matrix.

3.3 Information Matrix

The maximum likelihood method is a powerful method to search for modeled signals in noisy data. The formalism from both a statistical and geometric viewpoint has been developed and explored for use in LIGO data analysis by Finn [68], Cutler *et al.* [69], and Owen *et al.* [67, 70] among others. The maximum likelihood method is used to search for periodic sources in the data. The search statistic

using this method is the log-likelihood function Λ defined by

$$\ln \Lambda \equiv \langle h|u\rangle - \frac{1}{2}\langle u|u\rangle, \tag{3.12}$$

where h is the signal and u a template. The inner product, described in the previous section, on any two continuous real-valued functions $u(t), v(t)$ is defined by

$$\langle u|v\rangle = 4\Re \int_0^\infty df \frac{\widetilde{u}^*\,(f)\;\widetilde{v}\,(f)}{S_h(f)}, \tag{3.13}$$

where $\sim$ is used to denote Fourier transforms. The detection statistic is then defined as the maximum of $\ln \Lambda$ over the unknown parameters [71]. We will normalize the templates so that

$$\langle u(\lambda^\alpha)|u(\lambda^\alpha)\rangle = 1 \tag{3.14}$$

Now consider a point $\boldsymbol{\lambda}$ and a neighboring point $\boldsymbol{\lambda} + \Delta\boldsymbol{\lambda}$ where the separation between the two points is small in some sense. Then we can Taylor expand to second order to obtain

$$\langle u(\boldsymbol{\lambda} + \Delta\boldsymbol{\lambda})|u(\boldsymbol{\lambda})\rangle = 1 - \frac{1}{2}\Gamma_{\mu\nu}\Delta\lambda^\mu\Delta\lambda^\nu \tag{3.15}$$

where we have used two assumptions to simplify the result. The normalization constraint (3.14) was applied. Also, the fact that the inner product will be maximum when $\Delta\lambda^\alpha = 0$ implies that the first order term vanishes and the second order term is negative. The minus sign forces the the matrix formed from the coefficients $\Gamma_{\mu\nu}$ to be positive definite, and reflects the fact that, for a normalized signal, the signal-to-noise on the average decreases if the signal and template do not match.

The matrix $\Gamma_{\mu\nu}$ can be shown to be of the form [72]

$$\Gamma_{\mu\nu} = \langle \partial_\mu(\ln \Lambda(\boldsymbol{\lambda}))|\partial_\nu(\ln \Lambda(\boldsymbol{\lambda}))\rangle. \tag{3.16}$$

Therefore we identify $\Gamma_{\mu\nu}$ as the Fisher information matrix by definition. The derivation outlined so far is a general method not specific to periodic sources, and is outlined in greater detail by Finn [68].

An interesting property of the Fisher information matrix is that the inverse

is the covariance matrix $\Sigma^{\mu\nu}$. Not only can one use the information matrix to find the optimal method to search over a parameter space, but one can also use it to compute the measurement errors, covariances and correlations between the parameters. The other key property of the information matrix is that it is positive definite. This will be turn out to be important when exploring the geometric interpretation of the information matrix.

3.4 Geometric interpretation

Since the match M between two templates u and v defined by

$$M \equiv \langle u|v\rangle \tag{3.17}$$

is a measure of signal-to-noise, and signal-to-noise is manifestly invariant under reparametrization, the mismatch $1 - M$ can be interpreted as a measure of the proper distance (actually the square) between templates. This motivates identifying the Fisher information matrix as a metric on the parameter space. Now it will be shown formally that taking the Fisher information matrix to be the metric on the parameter space is mathematically justified.

The set of all possible outputs of the detector is a set that we will denote by V. Clearly the set is closed under addition, satisfies associativity, has a scalar multiplicative identity, and is distributive. We therefore conclude that V is a vector space. Notice that the possible outputs of a detector will be time series with the same sampling frequencies, and therefore the vector space is finite dimensional, but can be approximated with the continuum limit (i.e. infinite dimensional) due to how large $dim(V)$ is (*e.g.*, 16384 for one second of LIGO data).

The parameter space is defined as the set of all N-tuples $\{\lambda_0, \lambda_1, ...\lambda_{N-1}\} \subset \Re^N$. The template function is then defined to be the map $u : \Lambda \to V$. Each template associated with a point $p \in \Lambda$ is a vector in V given by the mapping $u(p) \in V$. Therefore we define the template space $\mathcal{T}$ to be the image of Λ under the u. The parameter space is separate from the function space. The two spaces are connected by a map u. A point in the parameter space Λ is an N-tuple, while the corresponding point on the template space $\mathcal{T}$ is a vector.

Vectors in V are time series. A discrete Fourier transform algorithm (DFT) is a numerical procedure for transforming these vectors into the frequency domain that approaches the Fourier transform in the continuum limit. The DFT maps V into a different space that we will denote by $\widetilde{V}$. Since the map DFT is linear and V is a vector space, then $\widetilde{V}$ is also a vector space. We will from now on denote $DFT(u)$ as $\widetilde{u}$ for all $u \in V$. The power spectral density S_h is a scalar field on the frequency domain. Since $\widetilde{V}$ is a complex vector space, we can define the inner product on $\widetilde{V}$ to be a weighted inner product as follows. The frequency domain is discretized into bins $\{f_{(j)}\}$. Each bin $\{f_{(j)}\}$ can be associated with a vector $e_j \in \widetilde{V}$ that form a basis on $\widetilde{V}$. Any vector $\widetilde{v} \in \widetilde{V}$ then has components $\{v_j\}$ in that basis. The inner product between two vectors $\widetilde{u}, \widetilde{v}$ in $\widetilde{V}$ will be defined to be

$$\widetilde{u} \cdot \widetilde{v} \equiv \sum_{f_{(j)}} \frac{u_j v_j}{S_h(f_{(j)})} \tag{3.18}$$

We will now define the inner product on V by

$$u \cdot v \equiv \widetilde{u} \cdot \widetilde{v} \tag{3.19}$$

$\forall u, v \in V$. LAL computes this as a finite sum, but notice that in the continuum limit this becomes the usual

$$\langle u|v\rangle = \int df \frac{\widetilde{u}^*(f)\,\widetilde{v}(f)}{S_h(f)} \tag{3.20}$$

where now $\widetilde{u}, \widetilde{v}$ is the continuous Fourier transform of u, v.

Now the proposed inner product must be shown to be well defined. By inspection, the proposed inner product is linear and symmetric, and the norm of any vector is non-negative. Therefore inner product on V is well defined.

Assume that the derivatives $\partial u/\partial\lambda^\alpha \equiv \partial_\alpha u$ for $\alpha = 0, 1, ..., N$ exist and are continuous. Then the collection of functions $\Gamma_{\alpha\beta} : \Lambda \to \Re$ for $\alpha, \beta = 0, 1, ..., N$ defined by

$$\Gamma_{\alpha\beta} \equiv \partial_\alpha u \cdot \partial_\beta u \tag{3.21}$$

are continuous functions on Λ.

It will now be shown that the object

$$\Gamma \equiv \Gamma_{\alpha\beta} d\lambda^{\alpha} \otimes d\lambda^{\beta} \tag{3.22}$$

can be taken to be the metric on Λ and is well defined.

It must be shown that Γ is a symmetric, non-degenerate tensor field of type $(0, 2)$ on Λ. It's clear from the definition that Γ is a multi-linear 2-form for each point in Λ, and that it is invariant under coordinate transformation. Therefore Γ is a tensor field of type $(0, 2)$ on Λ. It is clear from (3.21) that Γ is symmetric on the coordinate basis $\{\partial/\partial\lambda^{\alpha}\}$, for each point in Λ. Therefore Γ is symmetric on the tangent space $V_p, \forall p \in \Lambda$. Thus Γ is a symmetric tensor-field on Λ. Because the metric is identified as the Fisher information matrix, it has the additional property of being positive-definitive. It follows from that property that Γ is non-degenerate. Therefore Γ, the metric, is well defined.

A subspace of the full parameter space is what is used for the unknown pulsar search. This is because not all parameters are intrinsic to the astrophysical source. Those parameters that encode information about the astrophysical source are called intrinsic parameters, and will be labeled by $\boldsymbol{\lambda}$. Those that do not are called extrinsic parameters, and will be labeled by $\boldsymbol{\mu}$. The match M will be redefined on the subspace by

$$M = \max_{\boldsymbol{\mu}} \langle u(\boldsymbol{\mu}; \boldsymbol{\lambda}) | u(\boldsymbol{\mu} + \Delta\boldsymbol{\mu}; \boldsymbol{\lambda} + \Delta\boldsymbol{\lambda}) \rangle \tag{3.23}$$

and the metric g on that subspace will be defined from M, just as Γ was on the full parameter space. This is equivalent to projecting out the intrinsic parameters, and so the resulting equation relating g to Γ is given by

$$g_{ij} = \Gamma_{ij} - \Gamma_{im}\Gamma_{jn}\gamma^{mn}, \tag{3.24}$$

where γ_{mn} is the metric on the extrinsic parameter space, and γ^{mn} is the inverse. In the special case of only projecting out one parameter, label it 0, equation (3.24) becomes

$$g_{ij} = \Gamma_{ij} - \frac{\Gamma_{i0}\Gamma_{j0}}{\Gamma_{00}}. \tag{3.25}$$

This describes the general mathematical formalism of the information matrix. Now

let us see the exact form it has for the pulsar search.

3.5 The information matrix for pulsars

Monochromatic or periodic signals should only depend on the frequency evolution, and extrinsic parameters such as the phase offset and the amplitude. But the sources searched for are not quite monochromatic. The detector is in a rotating frame relative to pulsars. LIGO is stationary on Earth, but the Earth is spinning and orbiting around the Sun. Thus pulsars would appear to be Doppler shifted relative to the interferometers. The effect can be corrected for by transforming to an inertial coordinate system. These coordinates are called barycentric coordinates. The pertinent one is the time coordinate, which will be used to stretch the data to make a source look monochromatic. Let R_o be the orbital radius of Earth. Let R_s be the Earth's radius. The sky position will be described by the coordinates right ascension α and declination δ. The inclination angle between the rotation axis and the ecliptic is denoted by i. The latitude angle by λ. In terms of those variables, the coordinate transformation from detector time t to barycentric time t_b is given by

$$\begin{aligned} t_b = t &+ \cos\delta\cos\alpha\,[R_o\cos\phi_{orb} + R_s\cos\lambda\cos\phi_{spin}] \\ &+ \cos\delta\sin\alpha\,[R_o\cos i\sin\phi_{orb} + R_s\cos\lambda\sin\phi_{spin}] \\ &+ \sin\delta\,[R_o\sin i\sin\phi_{orb} + R_s\sin\lambda] \end{aligned} \tag{3.26}$$

which follows from the Doppler shift formula $t \rightarrow t + \boldsymbol{v}\cdot\boldsymbol{x}$. Here the orbit is approximated as circular with phase ϕ_{orb} and the Earth's rotational phase is ϕ_{spin}. Thus the motion of LIGO is epicyclic. This is called the *Ptolemaic* approximation.

The benefit of using the barycentric time coordinate is that pulsars will appear to be periodic sources within that frame. There is one remaining complication however. Pulsars are actually spinning down on timescales of hundreds of years or more, much longer than any LIGO data run. Thus it is justified to model the frequency evolution due to spindown with a Taylor expansion. And so we define the canonical time by

$$t_c = t_b + \frac{1}{2}f_1 T\frac{(t_b - t_0)^2}{T^2} \tag{3.27}$$

for one spindown parameter and

$$t_c = t_b + \sum_{k=1}^{N} \frac{f_k T^k}{k+1} \left(\frac{(t_b - t_0)}{T} \right)^{k+1} \tag{3.28}$$

in general, where t_0 is the starting time of the observation, and T is the duration. To rephrase, the slice of data being analyzed is said to be over the time interval $[t_0, t_0 + T]$. And the Taylor expansion is being used to model the frequency drift over that time interval.

The amplitude of the waveform is also modulated because the sensitivity of an interferometer is not isotropic, but rather depends on an antenna beam pattern. However this effect is small enough that the modulation of the amplitude can be neglected, as demonstrated by Prix [73]. Thus the amplitude will be treated as an extrinsic parameter, and is fixed by the normalization constraint of the templates. Finally we arrive at the form of the template. With the canonical time coordinate the template takes the form

$$u(\alpha, \delta, \phi, f, f_1, \ldots) \sim \cos\left(2\pi f t_c + \phi\right), \tag{3.29}$$

where the proportionality factor is not important due to the assumption of template normalization. The extrinsic parameters λ, i are really constants which can be absorbed into the definition of the phase. The observation time T is set before analysis is done on the data. T can then also be treated as a constant. Out of the remaining parameters, the phase offset ϕ and the amplitude are extrinsic parameters. Maximization and projection must be done over these parameters.

Defining $\psi \equiv 2\pi f t_c + \phi$ the information matrix is then proportional to

$$\Gamma_{\mu\nu} = \langle \partial_\mu \psi | \partial_\nu \psi \rangle. \tag{3.30}$$

Maximizing over the phase offset and setting the amplitude to unity we obtain the search metric

$$g_{\mu\nu} = \langle \partial_\mu \psi | \partial_\nu \psi \rangle - \langle \partial_\mu \psi \rangle \langle \partial_\nu \psi \rangle. \tag{3.31}$$

The orbital speed of Earth is $v_o/c \sim 10^{-4}$ and the frequency band of LIGO is $100 - 1000$ Hz. Thus the frequency of a pulsar is at most Doppler modulated by

$\pm.1$ Hz. This is a small enough interval that one can safely assume that the noise spectrum is flat over it. The inner products can then be evaluated by

$$\langle u|v\rangle = \int_{t_0}^{t_0+T} \frac{dt}{T} u^*(t)v(t) \tag{3.32}$$

which becomes

$$\langle u|v\rangle = \int_{t_0}^{t_0+T} \frac{dt}{T} u(t)v(t) \tag{3.33}$$

provided that u and v are real valued functions.

The remaining variables are the observation time T and the time offset t_0, and they are not treated as parameters to be searched over or maximized. They are determined by choosing the data slice to be analyzed. The description is complete, and the information matrix can be analytically computed now. The expressions were evaluated by assuming the slow motion approximation. The rotation and orbital motion of the Earth are not at relativistic speeds. These assumptions can be expressed as

$$v_s \sim R_s\omega_s \ll 1, \tag{3.34}$$

$$v_o \sim R_o\omega_o \ll 1, \tag{3.35}$$

in geometric units. The components of the metric will be Taylor expanded to second order in these variables.

Using the following expressions for ease (arbitrary quantity Q)

$$\Delta Q \equiv Q_{\text{final}} - Q_{\text{initial}}, \tag{3.36}$$

$$\Delta\phi_o \equiv \phi_{o,\text{final}} - \phi_{o,\text{initial}} = \omega_o T, \tag{3.37}$$

$$\Delta\phi_s \equiv \phi_{s,\text{final}} - \phi_{s,\text{initial}} = \omega_s T, \tag{3.38}$$

The expression $\Gamma_{\mu\nu} \equiv \langle \partial_\mu\psi|\partial_\nu\psi\rangle$ is then evaluated component by component on the parameter space $\{(\alpha, \delta, f, \phi, f_1, \ldots f_N)\}$ to be

$$\Gamma_{\phi\phi} = 1 \tag{3.39}$$

$$\Gamma_{\phi f} = \pi T \tag{3.40}$$

$$\Gamma_{\phi\alpha} = -2\pi f \cos\delta[A_1 \sin\alpha + A_2 \cos\alpha] \quad (3.41)$$

$$\Gamma_{\phi\delta} = 2\pi f[-A_1 \sin\delta \cos\alpha + A_2 \sin\delta \sin\alpha + A_3 \cos\delta] \quad (3.42)$$

$$\Gamma_{ff} = \frac{(2\pi T)^2}{3} \quad (3.43)$$

$$\Gamma_{f\alpha} = (2\pi)^2 f \cos\delta T[-B_1 \sin\alpha + B_2 \cos\alpha] \quad (3.44)$$

$$\Gamma_{f\delta} = (2\pi)^2 fT[-B_1 \sin\delta \cos\alpha - B_2 \sin\delta \sin\alpha + B_3 \cos\delta] \quad (3.45)$$

$$\Gamma_{\alpha\alpha} = 2(\pi f \cos\delta)^2[B_4 \sin^2\alpha + B_5 \sin 2\alpha + B_6 \cos^2\alpha] \quad (3.46)$$

$$\begin{aligned}\Gamma_{\alpha\delta} &= 2(\pi f)^2 \cos\delta[B_4 \sin\alpha \cos\alpha \sin\delta - B_5 \sin^2\alpha \sin\delta \\ &- B_7 \sin\alpha \cos\delta + B_5 \cos^2\alpha \sin\delta \\ &- B_6 \sin\alpha \cos\alpha \sin\delta + B_8 \cos\alpha \cos\delta]\end{aligned} \quad (3.47)$$

$$\begin{aligned}\Gamma_{\delta\delta} &= 2(\pi f)^2[B_4 \cos^2\alpha \sin^2\delta + B_6 \sin^2\alpha \sin^2\delta \\ &+ B_9 \cos^2\delta - B_5 \sin 2\alpha \sin^2\delta \\ &- B_8 \sin\alpha \sin 2\delta - B_7 \cos\alpha \sin 2\delta]\end{aligned} \quad (3.48)$$

$$\Gamma_{\phi f_k} = \frac{2\pi f T^{k+1}}{(k+1)(k+2)} \quad (3.49)$$

$$\Gamma_{ff} = \frac{(2\pi T)^2}{3} \quad (3.50)$$

$$\Gamma_{ff_k} = \frac{(2\pi)^2 T^{k+2} f}{(k+1)(k+3)} \quad (3.51)$$

$$\Gamma_{f_j f_k} = \frac{(2\pi fT)^2 T^{j+k}}{(j+1)(k+1)(j+k+3)} \quad (3.52)$$

$$\begin{aligned}\Gamma_{f_k\alpha} &= \frac{(2\pi f)^2}{(k+1)T}\{-\cos\delta \sin\alpha[R_o I^o_{k,c} + R_s \cos\lambda I^s_{k,c}] \\ &+ \cos\delta \cos\alpha[R_o \cos\iota I^o_{k,s} + R_s \cos\lambda I^s_{k,s}]\}\end{aligned} \quad (3.53)$$

$$\begin{aligned}\Gamma_{f_k\delta} &= \frac{(2\pi f)^2}{(k+1)T}\{-\sin\delta \cos\alpha[R_o I^o_{k,c} + R_s \cos\lambda I^s_{k,c}] \\ &- \sin\delta \sin\alpha[R_o \cos\iota I^o_{k,s} + R_s \cos\lambda I^s_{k,s}]\} \\ &+ \cos\delta[R_o \sin\iota I^o_{k,s} + R_s \sin\lambda \frac{T^{k+2}}{k+2}]\}\end{aligned} \quad (3.54)$$

where the intermediate quantities are

$$A_1 = R_o \frac{\Delta \sin\phi_o}{\Delta\phi_o} + R_s \cos\lambda \frac{\Delta \sin\phi_s}{\Delta\phi_s} \quad (3.55)$$

$$A_2 = R_o \cos i \frac{\Delta \cos \phi_o}{\Delta \phi_o} + R_s \cos \lambda \frac{\Delta \cos \phi_s}{\Delta \phi_s} \tag{3.56}$$

$$A_3 = -R_o \sin i \frac{\Delta \cos \phi_o}{\Delta \phi_o} + R_s \sin \lambda \tag{3.57}$$

$$A_4 = R_o \left[\frac{\sin \phi_{o,\text{final}}}{\Delta \phi_o} + \frac{\Delta \cos \phi_o}{(\Delta \phi_o)^2} \right] \tag{3.58}$$

$$A_5 = R_s \left[\frac{\sin \phi_{s,\text{final}}}{\Delta \phi_s} + \frac{\Delta \cos \phi_s}{(\Delta \phi_s)^2} \right] \tag{3.59}$$

$$A_6 = R_o \left[-\frac{\cos \phi_{o,\text{final}}}{\Delta \phi_o} + \frac{\Delta \sin \phi_o}{(\Delta \phi_o)^2} \right] \tag{3.60}$$

$$A_7 = R_s \left[-\frac{\cos \phi_{s,\text{final}}}{\Delta \phi_s} + \frac{\Delta \sin \phi_s}{(\Delta \phi_s)^2} \right] \tag{3.61}$$

$$A_8 = R_o^2 \left(1 + \frac{\Delta \sin 2\phi_o}{2\Delta \phi_o} \right) \tag{3.62}$$

$$A_9 = R_o R_s \left[\frac{\Delta \sin(\phi_o - \phi_s)}{\Delta \phi_o - \Delta \phi_s} + \frac{\Delta \sin(\phi_o + \phi_s)}{\Delta \phi_o + \Delta \phi_s} \right] \tag{3.63}$$

$$A_{10} = R_s^2 \left(1 + \frac{\Delta \sin 2\phi_s}{2\Delta \phi_s} \right) \tag{3.64}$$

$$A_{11} = R_o^2 \frac{\Delta \cos 2\phi_o}{2\Delta \phi_o} \tag{3.65}$$

$$A_{12} = R_o R_s \left[-\frac{\Delta \cos(\phi_o - \phi_s)}{\Delta \phi_o - \Delta \phi_s} + \frac{\Delta \cos(\phi_o + \phi_s)}{\Delta \phi_o + \Delta \phi_s} \right] \tag{3.66}$$

$$A_{13} = R_o R_s \left[\frac{\Delta \cos(\phi_o - \phi_s)}{\Delta \phi_o - \Delta \phi_s} + \frac{\Delta \cos(\phi_o + \phi_s)}{\Delta \phi_o + \Delta \phi_s} \right] \tag{3.67}$$

$$A_{14} = R_s^2 \frac{\Delta \cos 2\phi_s}{2\Delta \phi_s} \tag{3.68}$$

$$A_{15} = R_o^2 \left(1 - \frac{\Delta \sin 2\phi_o}{2\Delta \phi_o} \right) \tag{3.69}$$

$$A_{16} = R_o R_s \left[\frac{\Delta \sin(\phi_o - \phi_s)}{\Delta \phi_o - \Delta \phi_s} - \frac{\Delta \sin(\phi_o + \phi_s)}{\Delta \phi_o + \Delta \phi_s} \right] \tag{3.70}$$

$$A_{17} = R_s^2 \left(1 - \frac{\Delta \sin 2\phi_s}{2\Delta \phi_s} \right) \tag{3.71}$$

$$A_{18} = R_0 R_s \frac{\Delta \sin \phi_o}{\Delta \phi_o} \tag{3.72}$$

$$A_{19} = R_s^2 \frac{\Delta \sin \phi_s}{\Delta \phi_s} \tag{3.73}$$

$$A_{20} = R_0 R_s \frac{\Delta \cos \phi_o}{\Delta \phi_o} \tag{3.74}$$

$$
\begin{aligned}
A_{21} &= R_s^2 \frac{\Delta \cos\phi_s}{\Delta\phi_s} && (3.75)\\
B_1 &= A_4 + A_5 \cos\lambda && (3.76)\\
B_2 &= A_6 \cos i + A_7 \cos\lambda && (3.77)\\
B_3 &= A_6 \sin i + \frac{R_s \sin\lambda}{2} && (3.78)\\
B_4 &= A_8 + 2A_9 \cos\lambda + A_{10} \cos^2\lambda && (3.79)\\
B_5 &= A_{11} \cos i + A_{12} \cos\lambda + A_{13} \cos i \cos\lambda + A_{14} \cos^2\lambda && (3.80)\\
B_6 &= A_{15} \cos^2 i + 2A_{16} \cos i \cos\lambda + A_{17} \cos^2\lambda && (3.81)\\
B_7 &= -A_{11} \sin i + 2A_{18} \sin\lambda - A_{13} \sin i \cos\lambda + A_{19} \sin 2\lambda && (3.82)\\
B_8 &= A_{15} \sin i \cos i - 2A_{20} \cos i \sin\lambda + A_{16} \sin i \cos\lambda - A_{21} \sin 2\lambda && (3.83)\\
B_9 &= A_{15} \sin^2 i - 4A_{20} \sin i \sin\lambda + 2R_s^2 \sin^2\lambda && (3.84)\\
I_{k+1,c} &= \frac{T^{k+1}}{\omega} \sin\phi_{\text{final}} - \frac{k+1}{\omega^2} \left\{ -T^k \cos\phi_{\text{final}} + kI_{k-1,c} \right\} && (3.85)\\
I_{-1,c} &= \frac{\Delta \sin\phi}{\omega} && (3.86)\\
I_{0,c} &= T \frac{\sin\phi_{\text{final}}}{\omega} + \frac{\Delta \cos\phi}{\omega^2} && (3.87)\\
I_{k+1,s} &= -\frac{T^k}{\omega} \cos\phi_{\text{final}} + \frac{(k+1)}{\omega^2} \left\{ T^k \sin\phi_{\text{final}} - kI_{k-1,s} \right\} && (3.88)\\
I_{-1,s} &= -\frac{\Delta \cos\phi}{\omega} && (3.89)\\
I_{0,s} &= = -\frac{T}{\omega} \cos\phi_{\text{final}} + \frac{\Delta \sin\phi}{\omega^2} && (3.90)
\end{aligned}
$$

and the search metric is found by projecting out the phase offset

$$g_{\mu\nu} = \Gamma_{\mu\nu} - \Gamma_{\mu\phi}\Gamma_{\nu\phi}/\Gamma_{\phi\phi}. \qquad (3.91)$$

These expressions are coded in the `LALPtoleMetric()` function in the pulsar package.

3.6 Tiling the parameter space without spindown

Now that the pulsar search metric has been determined, tiling the parameter space will be explored in detail. The frequency is easy to maximize over when dealing with frequency domain data. Therefore its natural to relegate the frequency to the role of an extrinsic parameter. Thus we will project out the frequency leaving the smaller parameter space of $\{(\alpha, \delta, f_1, \ldots, f_N)\}$. Now consider the case without spindown parameters. The parameter space is now only the two dimensional sky. The geometry of this space can be illustrated by looking at the contours of constant mismatch, as is shown in Figure 3.1. The plots have been exaggerated to more easily illustrate the geometry. If the space was flat, one would expect to find circles. Instead we find ellipses whose orientations vary across the parameter space. One can now see why a uniform grid might not be the optimal method to tile the space. Figure 3.3 demonstrates how the tiling is done using an algorithm developed by T Creighton which uses PtoleMetric as input.

There are parameters that are set by the data analyst. These are the mismatch, the starting time, the detector (latitude and longitude matter to some extent), the duration or observation time and the maximum frequency. All but the starting time determine the size of the grid. The starting time can have a striking impact on the grid as well, in a different way. Figure 3.1 should be contrasted with Figure 3.2. Figure 3.2 is how the tiling should be done three months after the default starting time, which is used in Figure 3.1. The default starting time is set near the vernal equinox. This demonstrates the impact that the starting time t_0 has on the tiling. The reason that the pattern has shifted so is that the derivatives of the orbital velocity with respect to the sky angles $\boldsymbol{v}$ changes across the year. This is because the acceleration changes direction continuously. Thus the information matrix must depend on the starting time. And that means that the geometry of the sky parameter space depends on t_0.

A good test for the accuracy of the analytic approximation is to test it against the full Ephemeris timing function. This is also in LAL coded up by C Cutler. It is derived from J Taylor's TEMPO code for radio pulsar searches. To test both methods, both are used to compute the sky grid for the same value of the

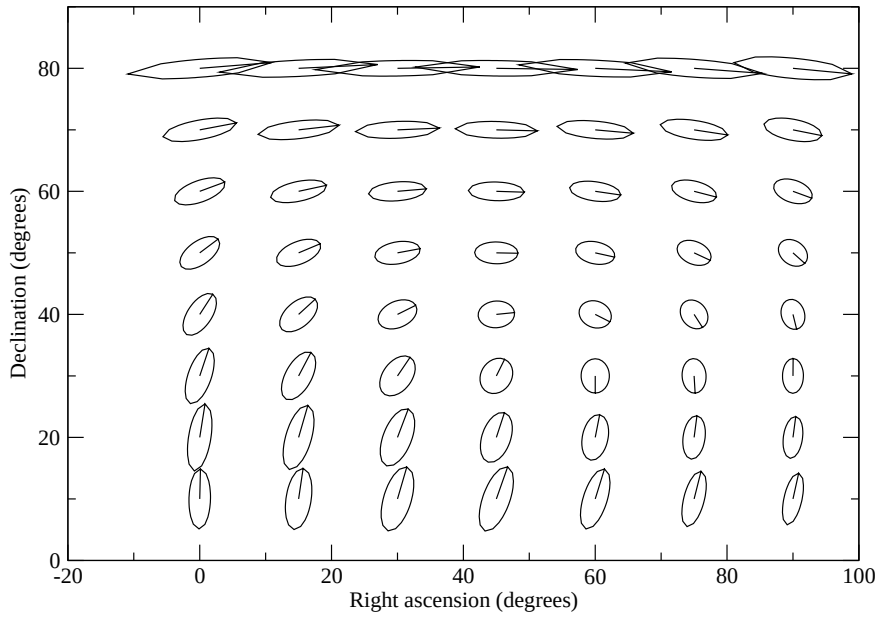

Figure 3.1. Ellipses of mismatch .02, illustrating the geometry of the parameter space for a sky only search.

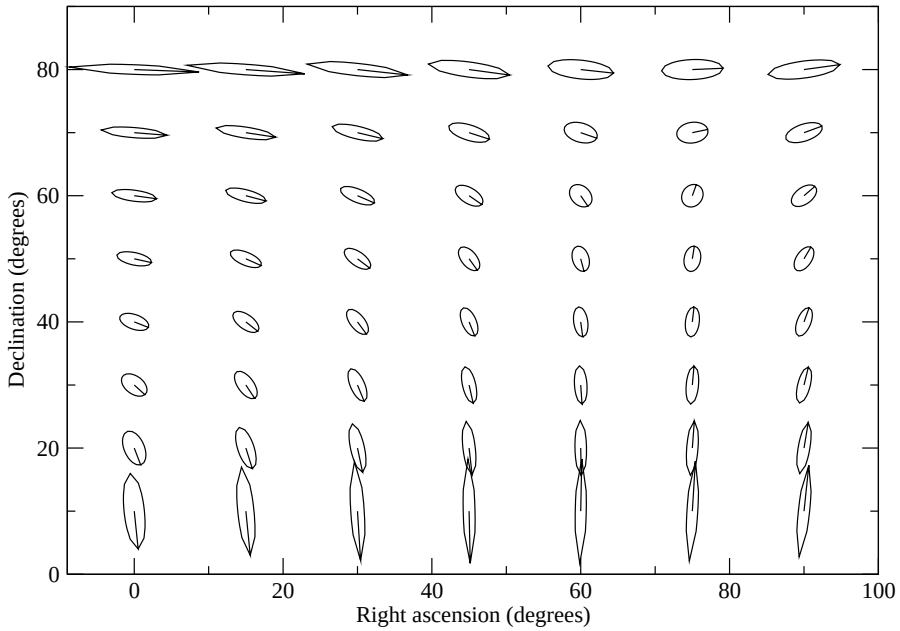

Figure 3.2. Ellipses for mismatch .02 three months past default start time.

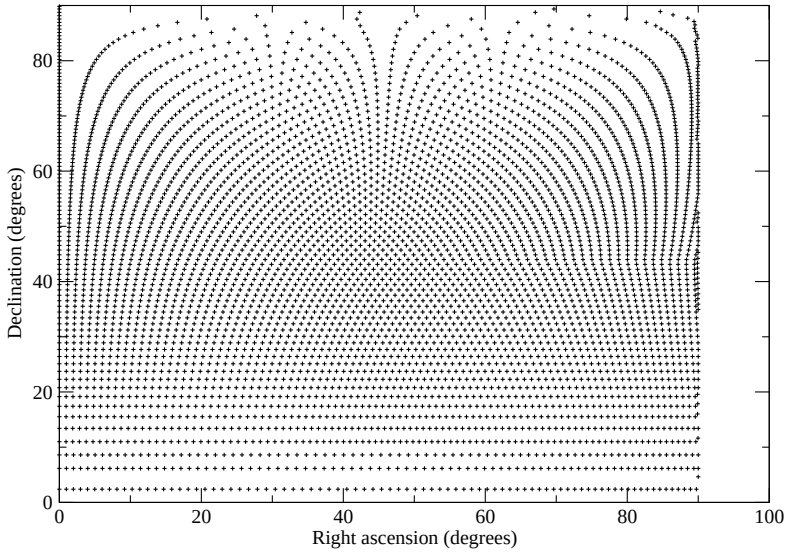

Figure 3.3. Tiling the sky for a mismatch of .2 using the analytic model.

mismatch, starting time, duration and maximum frequency parameters and then compared. Contrasting Figure 3.4 with Figure 3.5 the results are close, in fact all metric components are within ten percentage of each other. However, it look a little over a second to create the grid using the analytic method, while it took several hours using the Ephemeris data. This demonstrates that the analytic *Ptolemaic* approximation method is nearly as accurate as the full Ephemeris result, while being thousands of times faster.

The sky grid was tested with Monte Carlo simulations by Y Itoh to see how high the mismatch between randomly generated signals and the grid can be. The frequency was fixed, and only the sky parameters were explored. A small fraction had mismatches above .05 and they were all at the equator ($\delta = 0$). This was corrected by using a smaller mismatch (half the nominal size desired). The reason that this problem occurs is apparently due to neglecting the amplitude modulation. After these tests, PtoleMetric became the chosen code for Einstein@Home. It has been expanded to include spindown, which is now being used by Einstein@Home.

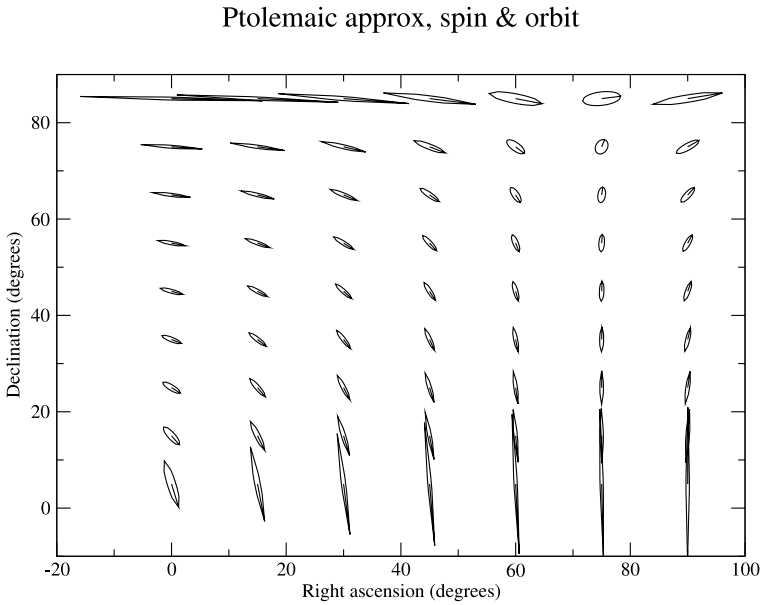

Figure 3.4. Mismatch ellipses for a mismatch of .02 and observation time of 11 hours for GEO using the Ptolemaic model, credit D I Jones

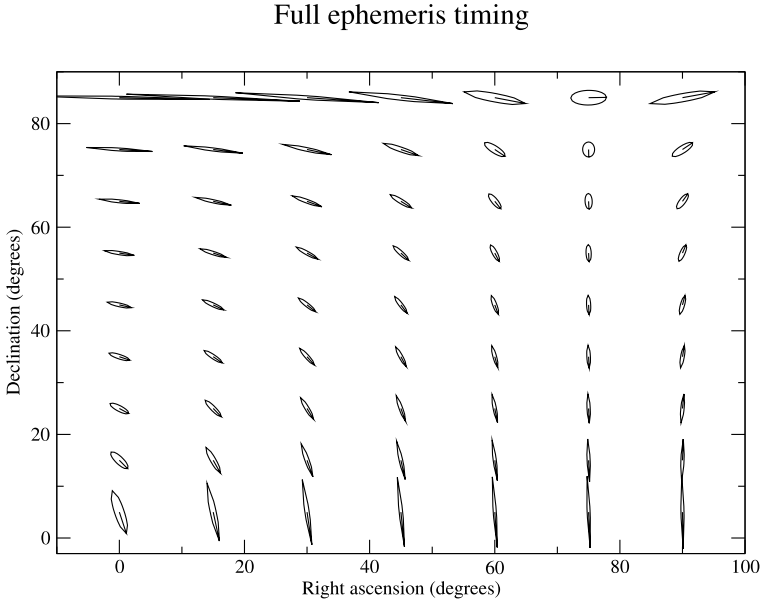

Figure 3.5. Mismatch ellipses using the same parameters as figure 3.4 using the Ephemeris timing function, credit D I Jones

3.7 Foliating the Parameter Space

For one spindown parameter, the tiling of the parameter space will now be determined. The tiling method was illustrated in the previous section for no spindown parameters. Knowing the tiling for the no spindown case will turn out to greatly simplify the case with nonzero spindown parameters. The inverse of the metric g is the covariance matrix Σ for the intrinsic parameters. Notice that

$$\Sigma^{\mu\nu} \cdot \boldsymbol{f_1}_\nu = \Sigma^{\mu 1} \approx \Sigma^{11} \boldsymbol{f_1}^\mu, \tag{3.92}$$

where $\boldsymbol{f_1}$ is the unit vector along the spindown axis. Equation (3.92) is true provided that

$$|\Sigma^{1\alpha}/\Sigma^{11}| \ll 1 \tag{3.93}$$

$$|\Sigma^{1\delta}/\Sigma^{11}| \ll 1. \tag{3.94}$$

Equations (3.93) and (3.94) have been found numerically to be true provided that roughly $T \gtrsim 10$ hours as in all Einstein@Home runs. Therefore we can conclude that $\boldsymbol{f_1}$ is approximately an eigenvector of Σ.

The covariance matrix Σ is real and symmetric. Also, it is obvious by inspection that the spindown eigenvalue is not equal to the other eigenvalues. Therefore the spindown eigenvector is orthogonal to the other eigenvectors. We will denote the normalized eigenvectors as $\{\boldsymbol{e_1}, \boldsymbol{e_2}, \boldsymbol{e_3}\}$, and identify $\boldsymbol{e_3} = \boldsymbol{f_1}$. Consequentially, the following must be true

$$1 - |\boldsymbol{e_1} \cdot \boldsymbol{f_1}| \ll 1 \tag{3.95}$$

$$1 - |\boldsymbol{e_2} \cdot \boldsymbol{f_1}| \ll 1 \tag{3.96}$$

which can and has also been confirmed numerically. Notice by inspection that the spindown eigenvalue is approximately Σ^{11} and that

$$\partial_\alpha \Sigma^{11} = 0 \tag{3.97}$$

$$\partial_\delta \Sigma^{11} = 0 \tag{3.98}$$

$$\partial_1 \Sigma^{\mu\nu} = 0 \tag{3.99}$$

Therefore the parameter space can be foliated by the slicing $\{(\alpha, \delta)\} \times \{f_1\}$. Since it is already known how to do the template placing on the subspace $\{(\alpha, \delta)\}$ the only remaining challenge is deciding on the number of divisions along $\boldsymbol{f_1}$. Note that due to equations (3.97),(3.98), (3.99) the spacing along the $\boldsymbol{f_1}$ axis will be uniform.

The grid without spindown is within 30% of the size predicted by Brady *et al.* [72]. The number of templates is higher than predicted because of the imperfections of realistic tiling. The scaling around a few days observation time was shown by Brady *et al.* to be complicated. There is no simple scaling relation when T is around the values that are typically used by Einstein@Home.

The argument that deduces that the foliation described above should be used relied heavily upon one assumption. Namely, the observation time can not be significantly less than a day. If the observation times are too short, degeneracy will lead to large correlations. The templates will start to look too alike at short observation times. This is why PtoleMetric was not used in the S2 all-sky search written up in [31]. For longer observation times, as will be the case for all subsequent analyses, PtoleMetric is used. The template spacing should be done by uniformly stacking sky grids orthogonal to the spindown axis. This result can be generalized for more spindown parameters. This means that the problem of template tiling for the LIGO pulsar search with spindown is reduced to the two dimensional problem of finding the optimal tiling for the sky parameters only. This tiling method with spindown has been validated by R Prix [73] through Monte Carlo simulations which expand on the results of Y Itoh (unpublished). Thus it is being used in present and future LIGO searches for periodic signals where computational cost is the restricting factor.

Bibliography

[1] Favata, M., S. A. Hughes, and D. E. Holz (2004) "How black holes get their kicks: Gravitational radiation recoil revisited," *Astrophys. J.*, **607**, pp. L5–L8, astro-ph/0402056.

[2] Merritt, D., M. Milosavljevic, M. Favata, S. A. Hughes, and D. E. Holz (2004) "Consequences of gravitational radiation recoil," *Astrophys. J.*, **607**, pp. L9–L12, astro-ph/0402057.

[3] Gultekin, K., M. C. Miller, and D. P. Hamilton (2004) "Growth of Intermediate-Mass Black Holes in Globular Clusters," *Astrophys. J.*, **616**, pp. 221–230, astro-ph/0402532.

[4] Fregeau, J. M., S. L. Larson, M. C. Miller, R. O'Shaughnessy, and F. A. Rasio (2006) "Observing IMBH-IMBH Binary Coalescences via Gravitational Radiation," astro-ph/0605732.

[5] Micic, M., T. Abel, and S. Sigurdsson (2005) "The Role of Primordial Kicks on Black Hole Merger Rates," astro-ph/0512123.

[6] Magain, P. et al. (2005) "Discovery of a bright quasar without a massive host galaxy," *Nature.*, **437**, pp. 381–384, astro-ph/0509433.

[7] Haehnelt, M. G., M. B. Davies, and M. J. Rees (2005) "Possible evidence for the ejection of a supermassive black hole from an ongoing merger of galaxies," astro-ph/0511245.

[8] Merritt, D. et al. (2006) "The nature of the HE0450-2958 System," *Mon. Not. Roy. Astron. Soc.*, **367**, pp. 1746–1750, astro-ph/0511315.

[9] Haiman, Z. (2004) "Constraints from Gravitational Recoil on the Growth of Supermassive Black Holes at High Redshift," *Astrophys. J.*, **613**, pp. 36–40, astro-ph/0404196.

[10] Volonteri, M. and M. J. Rees (2006) "Quasars at z=6: the survival of the fittest," astro-ph/0607093.

[11] Peres, A. (1962) "Classical Radiation Recoil," *Phys. Rev.*, **128**(5), pp. 2471–2475.

[12] Bekenstein, J. D. (1973) "Gravitational-radiation recoil and runaway black holes," *Astrophys. J.*, **183**, pp. 657–664.

[13] Fitchett, M. J. (1983) "The influence of gravitational wave momentum loss on the centre of mass motion of a Newtonian binary system," *Mon. Not. R. Astron. Soc.*, **203**, pp. 1049–1062.

[14] Fitchett, M. J. and S. Detweiler (1984) "Linear momentum and gravitational waves: circular orbits around a Schwarzschild black hole," *Mon. Not. R. Astron. Soc.*, **211**, pp. 933–942.

[15] Wiseman, A. G. (1992) "Coalescing binary systems of compact objects to (post)5/2 Newtonian order. 2. Higher order wave forms and radiation recoil," *Phys. Rev.*, **D46**, pp. 1517–1539.

[16] Kidder, L. E. (1995) "Coalescing binary systems of compact objects to postNewtonian 5/2 order. 5. Spin effects," *Phys. Rev.*, **D52**, pp. 821–847, gr-qc/9506022.

[17] Blanchet, L., M. S. S. Qusailah, and C. M. Will (2005) "Gravitational recoil of inspiralling black-hole binaries to second post-Newtonian order," *Astrophys. J.*, **635**, p. 508, astro-ph/0507692.

[18] Damour, T. and A. Gopakumar (2006) "Gravitational recoil during binary black hole coalescence using the effective one body approach," gr-qc/0602117.

[19] Baker, J. G. et al. (2006) "Getting a kick out of numerical relativity," astro-ph/0603204.

[20] Herrmann, F., D. Shoemaker, and P. Laguna (2006) "Unequal-Mass Binary Black Hole Inspirals," gr-qc/0601026.

[21] Ori, A. and K. S. Thorne (2000) "The transition from inspiral to plunge for a compact body in a circular equatorial orbit around a massive, spinning black hole," *Phys. Rev.*, **D62**, p. 124022, gr-qc/0003032.

[22] Bildsten, L. (1998) "Gravitational radiation and rotation of accreting neutron stars," *Astrophys. J.*, **501**, p. L89, astro-ph/9804325.

[23] Cutler, C. (2002) "Gravitational waves from neutron stars with large toroidal B-fields," *Phys. Rev.*, **D66**, p. 084025, gr-qc/0206051.

[24] Owen, B. J. (2005) "Maximum elastic deformations of compact stars with exotic equations of state," *Phys. Rev. Lett.*, **95**, p. 211101, astro-ph/0503399.

[25] Abbott, B. et al. (2006) "Search for gravitational wave bursts in LIGO's third science run," *Class. Quant. Grav.*, **23**, pp. S29–S39, gr-qc/0511146.

[26] Whelan, J. T. et al. (2005) "A data analysis technique for the LIGO-ALLEGRO stochastic background search," *Class. Quant. Grav.*, **22**, pp. S1087–S1096, gr-qc/0506025.

[27] Abbott, B. et al. (2006) "Search for gravitational waves from binary black hole inspirals in LIGO data," *Phys. Rev.*, **D73**, p. 062001, gr-qc/0509129.

[28] Owen, B. J. (2006) "Detectability of periodic gravitational waves by initial interferometers," *Class. Quant. Grav.*, **23**, pp. S1–S8.

[29] Lindblom, L., B. J. Owen, and S. M. Morsink (1998) "Gravitational radiation instability in hot young neutron stars," *Phys. Rev. Lett.*, **80**, pp. 4843–4846, gr-qc/9803053.

[30] Van Den Broeck, C. (2005) "The gravitational wave spectrum of non-axisymmetric, freely precessing neutron stars," *Class. Quant. Grav.*, **22**, pp. 1825–1840, gr-qc/0411030.

[31] Abbott, B. et al. (2006) "Coherent searches for periodic gravitational waves from unknown isolated sources and Scorpius X-1: Results from the second LIGO science run," gr-qc/0605028.

[32] ——— (2005) "Limits on gravitational wave emission from selected pulsars using LIGO data," *Phys. Rev. Lett.*, **94**, p. 181103, gr-qc/0410007.

[33] Brady, P. R. and T. Creighton (2000) "Searching for periodic sources with LIGO. II: Hierarchical searches," *Phys. Rev.*, **D61**, p. 082001, gr-qc/9812014.

[34] Krishnan, B. et al. (2004) "The Hough transform search for continuous gravitational waves," *Phys. Rev.*, **D70**, p. 082001, gr-qc/0407001.

[35] Dergachev, V. and K. Riles (2005), "LIGO Technical Document G050344-00-Z," .
URL http://admdbsrv.ligo.caltech.edu/dcc

[36] Abbott, B. et al. (2006) "Search for periodic gravitational waves with the LIGO detector," *in preperation*.

[37] Allen, B. (2005), "Einstein@Home S3 Analysis Summary," .
URL `http://einstein.phys.uwm.edu/PartialS3Results/`

[38] Thorne, K. S. and J. B. Hartle (1984) "Laws of motion and precession for black holes and other bodies," *Phys. Rev.*, **D31**, pp. 1815–1837.

[39] Tagoshi, H., A. Ohashi, and B. J. Owen (2001) "Gravitational field and equations of motion of spinning compact binaries to 2.5 post-Newtonian order," *Phys. Rev.*, **D63**, p. 044006, `gr-qc/0010014`.

[40] Blanchet, L. (2006), "Gravitational Radiation from Post-Newtonian Sources and Inspiralling Compact Binaries," .
URL `http://www.livingreviews.org/lrr-2006-4`

[41] Blanchet, L. and T. Damour (1986) "Radiative gravitational fields in general relativity I. general structure of the field outside the source," *Phil. Trans. Roy. Soc. Lond.*, **A320**, pp. 379–430.

[42] ——— (1988) "Tail transported temporal correlations in the dynamics of a gravitating system," *Phys. Rev.*, **D37**, p. 1410.

[43] ——— (1989) "Postnewtonian generation of gravitational waves," *Annales Poincare Phys. Theor.*, **50**, pp. 377–408.

[44] Damour, T. and B. R. Iyer (1991) "Multipole analysis for electromagnetism and linearized gravity with irreducible cartesian tensors," *Phys. Rev.*, **D43**, pp. 3259–3272.

[45] Blanchet, L. and T. Damour (1992) "Hereditary effects in gravitational radiation," *Phys. Rev.*, **D46**, pp. 4304–4319.

[46] Blanchet, L. (1995) "Second postNewtonian generation of gravitational radiation," *Phys. Rev.*, **D51**, pp. 2559–2583, `gr-qc/9501030`.

[47] Epstein, R. and R. Wagoner (1975) "Post-Newtonian generation of gravitational waves," *Astrophys. J.*, **197**, pp. 717–723.

[48] Wagoner, R. V. and C. M. Will (1976) "Postnewtonian gravitational radiation from orbiting point masses," *Astrophys. J.*, **210**, pp. 764–775.

[49] Wiseman, A. G. and C. M. Will (1991) "Christodoulou's nonlinear gravitational wave memory: Evaluation in the quadrupole approximation," *Phys. Rev.*, **D44**, pp. 2945–2949.

[50] Wiseman, A. G. (1993) "Coalescing binary systems of compact objects to (post)Newtonian**5/2 order. 4V: The Gravitational wave tail," *Phys. Rev.*, **D48**, pp. 4757–4770.

[51] Will, C. M. and A. G. Wiseman (1996) "Gravitational radiation from compact binary systems: gravitational waveforms and energy loss to second post- Newtonian order," *Phys. Rev.*, **D54**, pp. 4813–4848, gr-qc/9608012.

[52] Pati, M. E. and C. M. Will (2000) "Post-Newtonian gravitational radiation and equations of motion via direct integration of the relaxed Einstein equations. I: Foundations," *Phys. Rev.*, **D62**, p. 124015, gr-qc/0007087.

[53] Wald, R. M. (1984) *General Relativity*, The University of Chicago Press.

[54] Landau, L. D. and E. M. Lifshitz (1951) *The Classical Theory of Fields*, Reed Education and Professional Publishing, Boston.

[55] Thorne, K. S. (1980) "Multipole expansions of gravitational radiation," *Rev. Mod. Phys.*, **52**, pp. 299–339.

[56] Christodoulou, D. (1991) "Nonlinear nature of gravitation and gravitational wave experiments," *Phys. Rev. Lett.*, **67**, pp. 1486–1489.

[57] Chandrasekhar, S. (1983) *The Mathematical Theory of Black Holes*, Oxford University Press, New York.

[58] Glampedakis, K. and D. Kennefick (2002) "Zoom and whirl: Eccentric equatorial orbits around spinning black holes and their evolution under gravitational radiation reaction," *Phys. Rev.*, **D66**, p. 044002, gr-qc/0203086.

[59] Wilkins, D. C. (1972) "Bound Geodesics in the Kerr Metric," *Phys. Rev.*, **D5**, pp. 814–822.

[60] Blanchet, L. (2002) "Gravitational radiation from post-Newtonian sources and inspiralling compact binaries," *Living Rev. Rel.*, **5**, p. 3, gr-qc/0202016.

[61] Owen, B. J., H. Tagoshi, and A. Ohashi (1998) "Non-precessional spin-orbit effects on gravitational waves from inspiraling compact binaries to second post-Newtonian order," *Phys. Rev.*, **D57**, pp. 6168–6175, gr-qc/9710134.

[62] Blanchet, L., A. Buonanno, and G. Faye (2006) "Higher-order spin effects in the dynamics of compact binaries. II: Radiation field," gr-qc/0605140.

[63] Damour, T. (2001) "Coalescence of two spinning black holes: An effective one- body approach," *Phys. Rev.*, **D64**, p. 124013, gr-qc/0103018.

[64] Faye, G., L. Blanchet, and A. Buonanno (2006) "Higher-order spin effects in the dynamics of compact binaries. I: Equations of motion," gr-qc/0605139.

[65] Brandt, S. (1998) *Data Analysis: Statistical and Computational Methods for Scientists and Engineers*, Springer-Verlag, New York.

[66] Jaranowski, P., A. Krolak, and B. F. Schutz (1998) "Data analysis of gravitational-wave signals from spinning neutron stars. I: The signal and its detection," *Phys. Rev.*, **D58**, p. 063001, gr-qc/9804014.

[67] Owen, B. J. (1996) "Search templates for gravitational waves from inspiraling binaries: Choice of template spacing," *Phys. Rev.*, **D53**, pp. 6749–6761, gr-qc/9511032.

[68] Finn, L. S. (1992) "Detection, measurement and gravitational radiation," *Phys. Rev.*, **D46**, pp. 5236–5249, gr-qc/9209010.

[69] Cutler, C. and E. E. Flanagan (1994) "Gravitational waves from merging compact binaries: How accurately can one extract the binary's parameters from the inspiral wave form?" *Phys. Rev.*, **D49**, pp. 2658–2697, gr-qc/9402014.

[70] Owen, B. J. and B. S. Sathyaprakash (1999) "Matched filtering of gravitational waves from inspiraling compact binaries: Computational cost and template placement," *Phys. Rev.*, **D60**, p. 022002, gr-qc/9808076.

[71] Abbott, B. et al. (2004) "Setting upper limits on the strength of periodic gravitational waves using the first science data from the GEO 600 and LIGO detectors," *Phys. Rev.*, **D69**, p. 082004, gr-qc/0308050.

[72] Brady, P. R., T. Creighton, C. Cutler, and B. F. Schutz (1998) "Searching for periodic sources with LIGO," *Phys. Rev.*, **D57**, pp. 2101–2116, gr-qc/9702050.

[73] Prix, R. (2006) "Search for continuous gravitational waves: Metric of the multi-detector F-statistic," gr-qc/0606088.

Vita

David M Whitbeck

David M. Whitbeck was born on September 29, 1979 in Southfield, Michigan. He received his B.S. in Physics and Mathematics on June 2001 from the University of California at Davis. In the fall of 2001 he began graduate school at the Pennsylvania State University. He has been employed as a teaching assistant off and on for two years, and was recipient of the Roberts Fellowship from 2001-2002. For his contributions to the LSC, he will be on the author list for the next year. His other publications will include:

D. M. Whitbeck, B. J. Owen, Gravitational radiation recoil of spinning binary black hole mergers to second post-Newtonian order, *to be submitted for publication in Phys. Rev. D*